Instability of steady flows in helical pipes

Alexander Gelfgat [*]

School of Mechanical Engineering, Faculty of Engineering, Tel-Aviv University,
Ramat Aviv, Tel-Aviv 69978, Israel

A parametric numerical study of three-dimensional instability of steady flows in a helical pipe of arbitrary curvature and torsion is carried out. The computations are performed by a numerical approach verified against independent experimental and numerical results in a previous study. A possible power dependence of the friction factor on the Reynolds and Dean numbers is examined. The stability results are reported as dependences of the critical Reynolds number, critical wave number and the critical frequency on the dimensionless pipe curvature and torsion. A multiplicity of different disturbance modes becoming most unstable at different values of the governing parameters, is observed. Patterns of the most unstable modes are reported and classified. Different routes to instability including viscous and inviscid mechanisms, locally developing boundary and mixing layers, interaction between the Dean vortices, and the through flow are described.

I. INTRODUCTION

Instabilities of pressure gradient driven flows in helical pipes have been studied since the pioneering works of White and Taylor [1,2]. The fully developed steady flow in a helical pipe is noticeably more complicated than in a straight one, since the centrifugal and Coriolis forces induce additional spanwise vortical motion known as the Dean vortices. The Dean vortices necessarily appear in the helical pipe flow at any, even very small, pressure drop [3]. These vortices effectively mix either heat or mass without any need of additional mixing means, which resulted in their wide usage in various applications (see, e.g., Ref. [4]). Contrarily to flows in straight ducts, circular or rectangular, the helical pipe flow does not allow for an analytical solution for the steady base flow state, so that the numerical modeling is called for, even at low and moderate values of the Reynolds number. In this paper, we focus on examination of the stability of the calculated steady flows and computation of critical parameters at which the primary transition from steady to oscillatory flow takes place.

A particular interest in instabilities of the helical pipe flows is connected with the fact that unlike straight circular pipe flows, which have no linear stability limit [5], the helical pipe flows become linearly unstable at finite Reynolds numbers even at very small curvatures. Moreover, the computed and measured critical Reynolds numbers are very close starting from dimensionless curvature 0.01 [6,7], which shows that the transition takes place owing to the linear instability.

Assuming that helical pipe is infinite and has a uniform torsion, the flow is invariant regarding a position along the pipe center line. The latter allows for a two-dimensional solution for the base flow. The corresponding curvilinear orthogonal coordinates were proposed by Germano [8], which made fully nonlinear computations of steady helical pipe flows affordable [9–13]. Formulation in

---

[*]gelfgat@tau.ac.il

the Germano coordinates [8] is applied also in this study, which makes the base state dependent on only two coordinates. Periodicity of perturbations along the third coordinate is assumed. Calculation of the steady base flow and the linear stability analysis is carried out using the numerical approach described in Ref. [14], which is quite general for a two-dimensional steady base flow subject to three-dimensional infinitesimal disturbances that are periodic in one spatial direction.

Several researchers have studied instability onset in different helical pipes experimentally [1,2,15–20]. Most of the numerical studies of stability of helical pipes flows addressed either only two-dimensional disturbances [17], or only toroidal geometry [6,20,21], which is a limit case of a helical pipe with the zero torsion.

In our recent paper [7] we applied the numerical approach of Ref. [14] and established convergence of steady flows and eigenvalues of the linearized problem associated with their linear stability. An additional validation of calculated steady flows was obtained by comparison with the friction factors measured in Ref. [22]. Then we reviewed all cited above stability results and compared between them. It was shown that the results obtained using the present numerical technique agree well with the numerical results of Ref. [6] computed for a toroidal pipe, as well as with the experimental results of Refs. [18,19] obtained for the toroidal pipes and the helical pipes with small torsion. All the other experimental and numerical results cited above exhibit a considerable scatter and the reported critical Reynolds numbers are considerably larger than those reported in later experiments of Refs. [18,19]. In Ref. [7] we also could partially reproduce the experimental results of Ref. [17] obtained for large torsions, much larger than those applied in other experimental studies. Additionally, two examples of neutral stability curves for fixed values of the curvature and torsion were reported.

In this study we recall the convergence and validation studies reported in Ref. [7] and present an additional independent comparison with the friction factors measured in Ref. [23]. A computed series of dependencies of the friction factor on the Reynolds number allow us to address a "paradox" described in Ref. [24] and to show that there is no a "universal" power dependence of the friction factor on the Reynolds or Dean number. Then, basing on the established in Ref. [7] convergence of the steady flows and the eigenvalues of the linearized governing equations, we focus on parametric studies of instabilities of the helical pipe flows. These flows are defined by three governing parameters, the Reynolds number Re, the dimensionless curvature ε, and the dimensionless torsion τ of the pipe. As mentioned above, the linear stability of this flow in a toroidal pipe ($\tau = 0$) was studied in Ref. [6] and the results were verified against the experiments [18], and later numerically in Ref. [7]. Several examples of stability results for a nonzero torsion were presented in Ref. [7]; however, no systematic study where the torsion and the curvature are varied independently was ever published. In this study we expand the parameters range and report the stability results for the dimensionless pipe curvature and torsion varying in the intervals $0.01 \leqslant \varepsilon \leqslant 0.6$ and $0 \leqslant \tau/\varepsilon \leqslant 5$. To the best of the author's knowledge, such a parametric study is carried out for the first time.

The previous [6,7,17] and present studies of the linear stability of helical pipe flow showed that the primary instability sets in at the critical Reynolds number as a transition to a three-dimensional oscillatory flow. The instability is characterized additionally by the oscillation frequency ω_{cr}, the wave number k_{cr} that defines periodicity along the pipe center line, and the most unstable perturbation represented by the leading eigenvector of the linearized governing equations. It is a common place nowadays that in the course of a linear stability study, one observes several most unstable disturbances (perturbation modes) that replace each other with variation of the governing parameters. Several examples of that for convective and rotating flows can be found in Ref. [25]. In the considered ranges of the curvature and torsion, this study revealed 13 different most unstable perturbation modes replacing each other in the (ε, τ) plane.

In this study we make an attempt to classify the computed perturbation modes, to describe their features, and to offer, at least hypothetically, an explanation for possible physical mechanisms that lead to the onset of instability. Slightly supercritical three-dimensional flows are visualized in the cross-pipe planes using the divergence free projection approach of Ref. [26]. We observe that in different flow configurations, the instability sets in either in both Dean vortices, or only one of
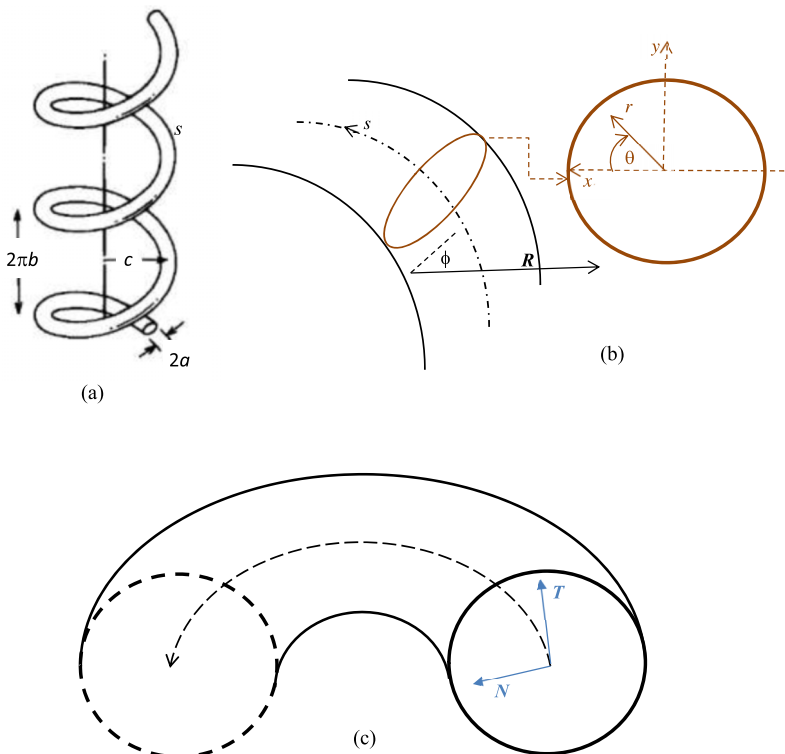
FIG. 1. Sketch of a helical pipe (left) and illustration of helical coordinates introduced by Germano [8]. Directions of the coordinate axes *x, y, r,* and θ correspond to those introduced in Refs. [8,28].

them, sometimes altering the whole vortex and sometimes only in a boundary layer. In some cases we observe instabilities arising in locally developing viscous boundary layers, while in other cases we observe an inviscid instability of local mixing layer configurations. The number of possible most unstable modes grows with the increase of the pipe curvature. This multiplicity of different patterns necessitates a large amount of graphical representations, which are supplied by animation files [27]. The latter helps to understand the structure of most unstable perturbations, and to visualize slightly supercritical flows.

II. FORMULATION OF THE PROBLEM

A. Coordinate system

To orthogonal coordinates of Germano [8] are based on the parametric definition of a helical curve

$$\boldsymbol{R}_0(t) = \{x(t), y(t), z(t)\} = \{c\cos(t), c\sin(t), bt\},\tag{1}$$

where c is the radius of the helix, $2\pi b$ is distance between coils (see Fig. 1), and t is a parameter. Its curvature κ and torsion τ are defined as

$$\kappa = \frac{c}{b^2 + c^2}, \quad \tau = \frac{b}{b^2 + c^2}.\tag{2}$$

Their ratio is $\lambda = \tau/\kappa = b/c$.

Starting from a toroidal pipe, which is a particular case of the helical pipe with zero torsion, we note that the same local polar coordinates can be defined in every cross section [6,11]. The third

orthogonal coordinate is a position along the pipe center line s. To preserve this orthogonality for an arbitrary helical pipe of the uniform torsion τ, position of the zero polar angle $\theta = 0$ (Fig. 1) must be varied along the pipe center line as

$$\xi = \theta - \int_{s_0}^{s} \tau \, ds = \theta - \tau(s - s_0). \tag{3}$$

The resulting coordinate system (r, ξ, s) is orthogonal. The Lamé coefficients of these coordinates are $H_r = 1$, $H_\xi = r$, $H_s = 1 + kr\sin(\xi)$. Assuming that the three fluid velocity components and the pressure are independent of the position at the pipe center line, i.e., independent of s, we arrive at a two-dimensional formulation for the velocity and the pressure of the base flow dependent only on r and ξ.

Consider a flow of incompressible fluid in a helical pipe of inner radius a, radius of coil c, and a constant distance between the coils equal to $2\pi b$. The pipe is sketched in Fig. 1(a). Figures 1(b) and 1(c) help to understand the arrangement of the coordinate system for a helix [Fig. 1(b)] and for a particular case of torus [Fig. 1(c)]. In the plane occupied by the torus center line we define a system of polar coordinates (R, ϕ), which produces also a system of Cartesian coordinates $X = R\cos(\phi)$, $Y = R\sin(\phi)$. The latter is not shown in the figure, but its location is obvious. The tangent to the center line is defined by $\boldsymbol{T} = d\boldsymbol{R}/ds = -\boldsymbol{e}_X\sin(\phi) + \boldsymbol{e}_Y\cos(\phi)$, and the normal $\boldsymbol{N} = \boldsymbol{R}d\boldsymbol{T}/ds = -\boldsymbol{e}_X\cos(\phi) - \boldsymbol{e}_Y\sin(\phi)$. These vectors are shown in Fig. 1(c). Now, in the normal to the center line cross section of the torus, we define a local Cartesian system so that the axes x and y are parallel to the vectors $\boldsymbol{N}$ and $\boldsymbol{T}$, respectively. This brings us to the system of coordinates introduced by Wang [28] and then used by Germano [8]. The resulting system of coordinates is the position along the center line s, and the polar coordinates r and ξ in the pipe cross section, where the zero position of ξ depends on the position s according to Eq. (3). It is depicted in Fig. 1(b).

B. Governing equations

The flow is driven by a pressure gradient $dP/ds = G$, which is constant along the pipe center line and is governed by the continuity and momentum equations. The three dimensionless parameters defining the problem are the dimensionless curvature $\varepsilon = a\kappa$, the torsion to curvature ratio λ, and the Reynolds number $\mathrm{Re}_d = \bar{U}d/\nu$, where $d = 2a$ is the pipe diameter, ν is the kinematic viscosity, and $\bar{U}$ is the flow mean velocity. The Dean number $\mathrm{De}_d = \mathrm{Re}_d\sqrt{\varepsilon}$ sometimes replaces the Reynolds number.

As explained in Refs. [7,11], the above definition of the Reynolds number requires the mean velocity value. This is convenient for experimental studies, however, in a numerical study, the mean velocity can be found only after calculation of the flow. For an alternative nondimensionalization, the pressure gradient based scales introduced in Refs. [7,11] are applied. The scales of length, time, velocity, and pressure are defined as a, $(\rho a/G)^{1/2}$, $(Ga/\rho)^{1/2}$, and Ga, respectively. The resulting system of the dimensionless continuity and momentum equations reads [recall that $H_s = 1 + kr\sin(\xi)$]

$$\nabla \cdot \boldsymbol{v} = 0, \quad \frac{\partial \boldsymbol{v}}{\partial t} + (\boldsymbol{v} \cdot \nabla)\boldsymbol{v} = -\frac{1}{H_s}\boldsymbol{e}_s - \nabla p + \frac{1}{R_G}\Delta\boldsymbol{v}, \tag{4,5}$$

where the dimensionless parameter $R_G = (Ga^3/\rho\nu^2)^{1/2}$ replaces the Reynolds number. The no-slip condition is posed on the pipe wall. The resulting Reynolds number is calculated as $\mathrm{Re}_d = 2\bar{V}_G R_G$, where $\bar{V}_G$ is the dimensionless average velocity obtained using the above formulation. All further details can be found in Ref. [7]. The governing equations for each velocity component are listed in Appendix. For the further visualization purposes we mention only the pseudo-streamfunction ψ defined as

$$v_r = \frac{1}{rH_s}\frac{\partial[H_s\psi]}{\partial\xi}, \quad v_\xi - \frac{\varepsilon\lambda r}{H_s}v_s = -\frac{1}{H_s}\frac{\partial[H_s\psi]}{\partial r}. \tag{6}$$

In the following, the velocity component v_s is called center line velocity, and part of the flow described by the pseudo-streamfunction is called cross-sectional flow. The Dean vortices corresponding to the negative and positive values of ψ are called "negative vortex" and "positive vortex," respectively. In the plane chosen for plots, the motion in negative vortices is counter-clockwise, while the motion in positive vortices is clockwise. Also, in all plots and animations below the blue color corresponds to the smallest values of depicted functions, and the red color to the largest values. Thus, negative and positive vortices can be distinguished by the blue or the red in their cores.

The linear stability of the calculated steady flows is studied assuming three-dimensional infinitesimally small disturbances that are periodic along the pipe center line direction s. The perturbations were represented in the form $\{\tilde{\boldsymbol{v}}(r, \xi), \ \tilde{p}(r, \xi)\}\exp[\sigma t + iks]$, where σ is the complex growth rate, k is the wave number along the center line, and tildes denote the infinitesimally small variables. The linearization procedure is straightforward and is described in Ref. [7]. The corresponding linearized equations are listed in Appendix.

The linear stability problem reduces to the generalized eigenvalue problem

$$\sigma \mathbf{B}(\tilde{\boldsymbol{v}}, \ \tilde{p})^T = \mathbf{J}(\tilde{\boldsymbol{v}}, \ \tilde{p})^T, \tag{7}$$

where $\mathbf{J}$ is the complex Jacobian matrix and $\mathbf{B}$ is the diagonal matrix such that its diagonal elements corresponding to the time derivatives of $\tilde{\boldsymbol{v}}$ are equal to one, while the elements corresponding to $\tilde{p}$ and the boundary conditions are zeros. Since the matrix $\mathbf{B}$ is singular, the generalized eigenproblem (7) is treated in the shift-and-inverse formulation, as described in Ref. [14].

III. NUMERICAL TECHNIQUE AND TEST CALCULATIONS

The continuity and momentum equations were discretized on staggered grids using central finite differences with linear interpolation between the nodes where necessary. Steady flows were calculated by Newton iteration in the same way as in Ref. [14].

Study of the stability of an s-independent two-dimensional steady flow for a given set of the governing parameters proceeds in the following way. For a fixed value of the wave number k we vary the complex shift σ_0, calculating each time 10–20 eigenvalues closest to the shift, until the eigenvalue σ of the eigenproblem (7) having the largest real part is found. This process is repeated for different values of the wave number k until the eigenvalue $\hat{\sigma}$ having the largest real part for all real wave numbers k is computed. This eigenvalue is called the leading eigenvalue. If $\text{Real}[\hat{\sigma}] = \max_k\{\text{Real}[\sigma(k)]\} > 0$ then the steady flow is unstable. Our purpose is to find the critical value of the number $R_{G,\text{cr}}$, dependent on ε and λ, at which $\text{Real}[\hat{\sigma}(k_{\text{cr}})] = 0$, where k_{cr} is the critical wave number, at which the above equality holds. In all the calculations described below the imaginary part of $\hat{\sigma}$ was nonzero. It estimates the frequency of appearing oscillations, is called critical frequency, and is denoted as $\hat{\omega}_{\text{cr}} = \text{Im}[\hat{\sigma}(R_{G,\text{cr}})]$. The corresponding eigenvector of (7) is called the leading eigenvector. It defines the most unstable perturbation of the base state and is used below for visualization of slightly supercritical flow states. Thus, the result of the stability study is given by the three critical values $R_{G,\text{cr}}$, k_{cr}, $\hat{\omega}_{\text{cr}}$ and the leading eigenvector, all dependent on the geometrical governing parameters ε and λ. To fit the traditional scaling, the results below are reported for $\text{Re}_{\text{cr}} = 2\bar{V}_G R_{G,\text{cr}}$, and the dimensionless critical frequency scaled by $(2a)/\bar{U}$, $\bar{\omega}_{\text{cr}} = 4\hat{\omega}_{\text{cr}}R_{G,\text{cr}}/\text{Re}_{\text{cr}}$. Since the perturbation at the critical point is proportional to $\exp[i\hat{\omega}_{\text{cr}}t + ik_{\text{cr}}s] = \exp[ik_{\text{cr}}(s - ct)]$, where $c = -\hat{\omega}_{\text{cr}}/k_{\text{cr}}$ is the phase speed of the developing traveling wave. Assuming $k_{\text{cr}} > 0$, the wave propagates downstream when $\hat{\omega}_{\text{cr}} < 0$ and $c > 0$, and upstream if $\hat{\omega}_{\text{cr}} > 0$ and $c < 0$.

The eigenproblem (7) is solved by the Arnoldi method. The shift-and-inverse formulation is provided by the ARPACK package [29] of Lechouq *et al.* Following Ref. [14], we calculate LU decomposition of the complex matrix $(\mathbf{J} - \sigma_0\mathbf{B})^{-1}$, so that calculation of the next Krylov vector for the Arnoldi method is reduced to one backward and one forward substitution. It should be noted that the Jacobian matrices for the Newton iteration and the stability analysis are different, since the
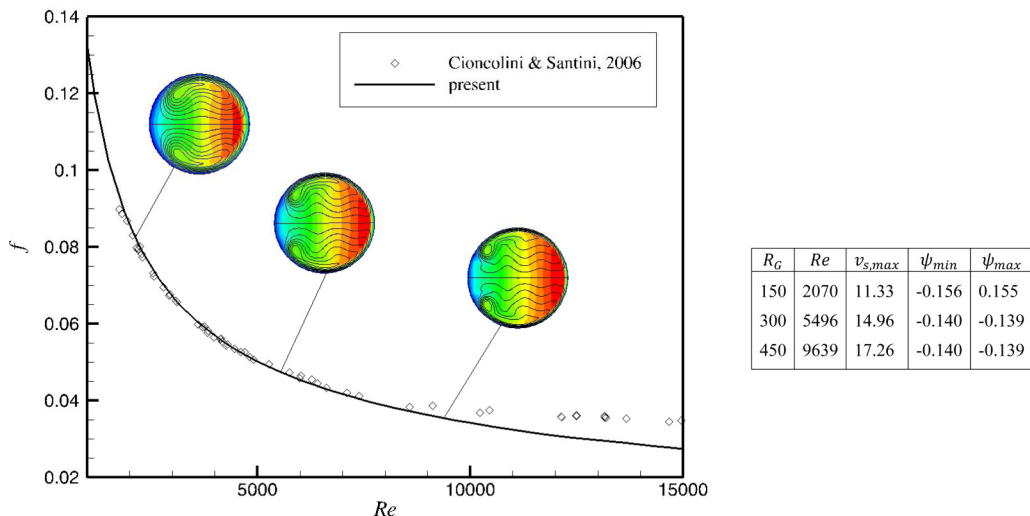
FIG. 2. Comparison of the friction factors measured in Ref. [23] and calculated in the present study. The experiment denoted as Coil_02, with $\varepsilon = 0.059256$ and $\lambda = 0.050128$ is chosen for the comparison. Inserts show isolines of the s velocity v_s (color plots) and pseudo-streamfunction ψ (black lines) at several characteristic points. The corresponding values of R_G and Re, as well as maximal values of v_s and maximal and minimal values of ψ, are shown in the table. All the isolines are equally spaced.

latter contains the terms depending on the wave number k that can also be complex. The Jacobian matrices were calculated directly from the numerical schemes.

The test calculations are reported in Ref. [7]. Below we report an additional independent comparison with the experimental results of Ref. [23] and address the paradox discussed in Ref. [24] regarding a possible power dependence of the friction factor on the Reynolds or Dean number. Comparing the calculated critical Reynolds numbers with the experimentally measured ones [7], we obtained a good agreement with the recent experiments [18,19] done for $\varepsilon < 0.1$ and $\lambda < 0.05$. Several earlier experiments that studied the instability onset for similar pipe curvatures and small torsions [1,2,14,16] found noticeably larger critical Reynolds numbers, and possibly missed the primary instability. A possible overestimation of the critical Reynolds number can be observed by comparison of Fig. 2 and the results reported below. The critical Reynolds number calculated for the parameters of Fig. 2 by the above described linear stability analysis is approximately 3525, while judging by the friction factor dependence (Fig. 2), it can be estimated to be above 8000.

IV. RESULTS

A. Steady flows and friction factors

Figures 2 and 3 compare the friction factors f of the helical pipe flows measured in Refs. [22,23] and computed in the present study. Similarly to the comparison with the measurements of Ref. [22] reported in Ref. [7], an example shown in Fig. 2, showing the comparison with the measurements of Ref. [23], we observe that the measured and calculated friction factors are close up to Re $\leqslant 8000$ and start to diverge at larger values. This disagreement is due to the turbulent flow regime, at which the friction factor is expected to be larger than that yielded by the laminar model. To illustrate how the flow pattern changes with the increase of the Reynolds number, several calculated steady flows are included in Fig. 2 as inserts. In these frames, as well as in all the figures below, it is assumed that the central axis of the helix (Fig. 1) is located on the left-hand side from every pipe cross section plotted, so that the inner pipe boundary corresponds to the left point of a plot border. For more information on the steady flow patterns the reader is referred to Ref. [7] and references therein.

TABLE I: Ranges of λ, at which the modes denoted on Figs. 5(b) and 5(c) were found.

Mode	ε	Range of λ	Mode characteristics	Perturbation animation	Flow animation
1	0.01	$0 \leqslant \lambda \leqslant 2.87$	Antisymmetry-breaking Dean vortices oscillate in counter phase Zero pseudo streamline is strongly perturbed An increase of through flow intensifies the Dean vortices, which slow down the through flow and consequently weaken by themselves	Perturbation_e=0p01_l=0.avi Perturbation_e=0p01_l=2.avi	Flow_e=0p01_l=0.avi Flow_e=0p01_l=2.avi
2	0.01	$2.87 \leqslant \lambda \leqslant 5$	Perturbations are located inside	Perturbation_e=0p01_l=4.avi	Flow_e=0p01_l=4.avi
	0.03	$1.1 \leqslant \lambda \leqslant 5$	a weaker vortex and are advected	Perturbation_e=0p05_l=4.avi	Flow_e=0p05_l=4.avi
	0.05	$1 \leqslant \lambda \leqslant 5$	along the streamlines	Perturbation_e=0p1_l=3p5.avi	Flow_e=0p1_l=3p5.avi
	0.075	$1.9 \leqslant \lambda \leqslant 5$	Zero pseudo streamline is strongly		
	0.1	$2.8 \leqslant \lambda \leqslant 4.2$	perturbed Instability of V_ξ boundary layer is assumed		
3	0.03	$0 \leqslant \lambda \leqslant 1.1$	Antisymmetry-preserving	Perturbation_e=0p03_l=0.avi	Flow_e=0p03_l=0.avi
	0.05	$0 \leqslant \lambda \leqslant 1$	Zero pseudo streamline is not perturbed	Perturbation_e=0p03_l=1.avi	Flow_e=0p03_l=1.avi
	0.075	$0 \leqslant \lambda \leqslant 0.9$	Dean vortices oscillate in phase and do not interact	Perturbation_e=0p05_l=0.avi Perturbation_e=0p075_l=0.avi	Flow_e=0p05_l=0.avi Flow_e=0p075_l=0.avi
	0.1	$0 \leqslant \lambda \leqslant 0.6$	Instability of V_ξ boundary layer is assumed	Perturbation_e=0p1_l=0.avi	Flow_e=0p1_l=0.avi
4	0.075	$0.9 \leqslant \lambda \leqslant 1.9$	Small circumferential wavenumber		
	0.1	$0.6 \leqslant \lambda \leqslant 2.8$	downstream cross-flow wave located inside	Perturbation_e=0p1_l=1p5.avi	Flow_e=0p1_l=1p5.avi
	0.2	$0.4 \leqslant \lambda \leqslant 2.55$	a weaker vortex Zero pseudo streamline is strongly perturbed	Perturbation_e=0p2_l=1p5.avi	Flow_e=0p2_l=1p5.avi

TABLE I: (*Continued.*)

| Mode	ε	Range of λ	Mode characteristics	Perturbation animation	Flow animation
5	0.1	$4.2 \leqslant \lambda \leqslant 5$	Large circumferential	Perturbation_e=0p1_l=4p5.avi	Flow_e=0p1_l=4p5.avi
	0.2	$2.55 \leqslant \lambda \leqslant$	wavenumber	Perturbation_e=0p2_l=3.avi	Flow_e=0p2_l=3.avi
	0.3	$5 \ 2.6 \leqslant \lambda \leqslant$	upstream cross-flow	Perturbation_e=0p2_l=4.avi	Flow_e=0p2_l=4.avi
	0.4	$2.88 \ 2.2 \leqslant$	wave	Perturbation_e=0p2_l=5.avi	Flow_e=0p2_l=5.avi
		$\lambda \leqslant 2.35$	Zero pseudo	Perturbation_e=0p3_l=2p7.avi	Flow_e=0p3_l=2p7.avi
			streamline, if exists, is	Perturbation_e=0p4_l=2p3.avi	Flow_e=0p4_l=2p3.avi
			strongly perturbed		
6	0.2	$0 \leqslant \lambda \leqslant 0.4$	Antisymmetry-breaking	Perturbation_e=0p2_l=0.avi	Flow_e=0p2_l=0.avi
	0.3	$0 \leqslant \lambda \leqslant 1.37$	Dean vortices do not interact	Perturbation_e=0p3_l=0.avi	Flow_e=0p3_l=0.avi
	0.4	$0 \leqslant \lambda \leqslant 0.7$	Zero pseudo streamline is weakly perturbed	Perturbation_e=0p3_l=1.avi	Flow_e=0p3_l=1.avi
	0.5	$0 \leqslant \lambda \leqslant 0.81$	At larger \lambda perturbations are located	Perturbation_e=0p4_l=0.avi	Flow_e=0p4_l=0.avi
	0.6	$0 \leqslant \lambda \leqslant 0.3$	inside a stronger vortex An inviscid instability of through flow is assumed	Perturbation_e=0p5_l=0.avi Perturbation_e=0p6_l=0.avi	Flow_e=0p5_l=0.avi Flow_e=0p6_l=0.avi
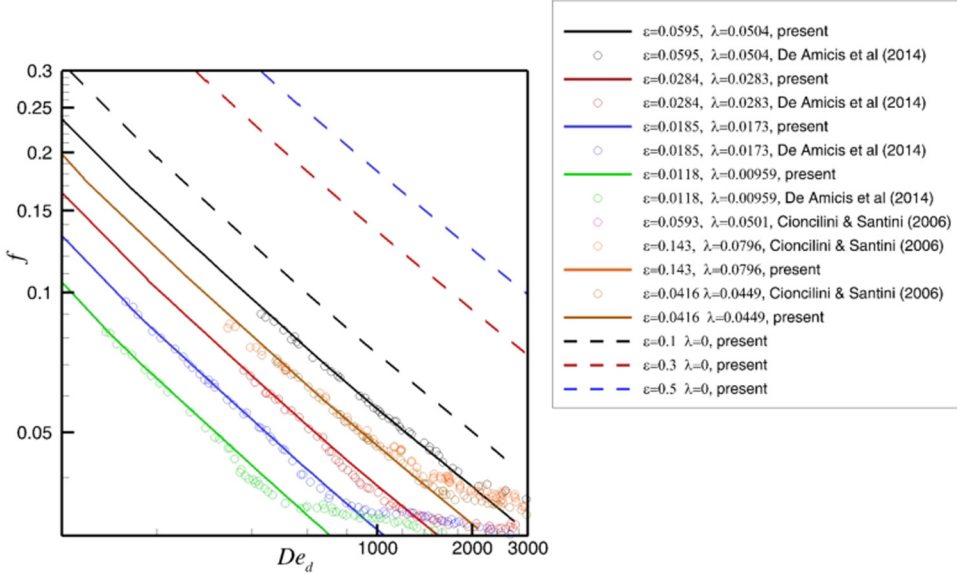
FIG. 3. Comparison of the friction factors measured in Refs. [22,23] in pipes with different curvature and torsion with those calculated in the present study.
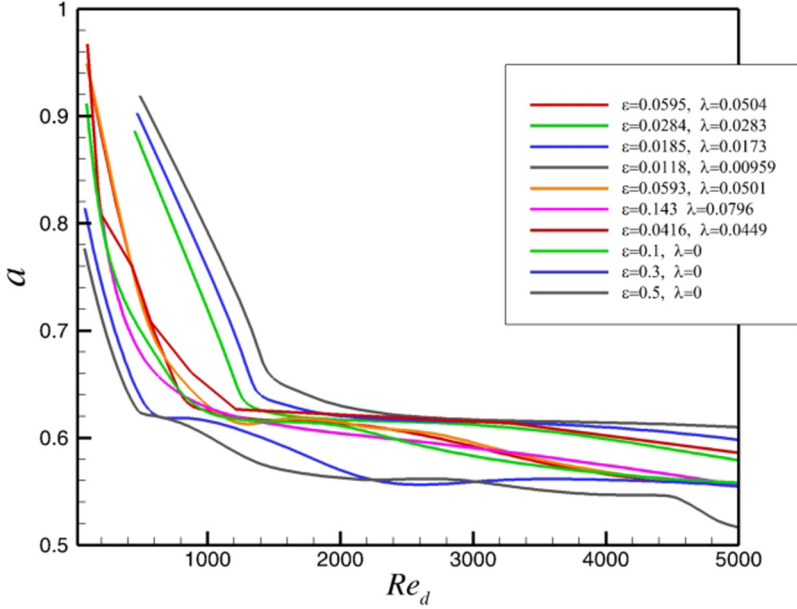
FIG. 4. Dependence of the exponent a on the Reynolds number for the cases shown in Fig. 2.

Figure 3 collects all the comparisons made with additional calculations for the toroidal pipe with $\varepsilon = 0.1,\ 0.3,\ 0.5$ and $\lambda = 0$. To address the "paradox" discussed in Ref. [24], the results are shown in the logarithmic scale and the Reynolds number is replaced by the Dean number. Comparing the experimental and numerical results we arrive to the above made conclusion: the measured and calculated friction numbers are in a good agreement until the Reynolds (Dean) number exceeds the value corresponding to the laminar-turbulent transition. A good agreement between the calculated and measured friction factors observed at moderate Dean and Reynolds numbers, $\mathrm{Re}_d \leqslant 5000$ and $\mathrm{De}_d \leqslant 700$, allows us to derive some more conclusions on the friction factor dependence on the Dean and Reynolds numbers.

The authors of study [24] questioned whether the ratio of friction factors in the coiled and the straight pipe f/f_s vary proportionally to $\mathrm{De}_d^{0.25}$, as was predicted by several analytical studies, or proportionally to $\mathrm{De}_d^{0.5}$, as resulted from several experiments and numerical studies. Since $f_s = 64/\mathrm{Re}_d$, we have to examine whether at constant dimensionless curvature ε the calculated friction factor behaves as Re_d^{-a}, and what is the value of the exponent a. For each $\varepsilon = \mathrm{const}$, the Dean number would exhibit the same power dependence, and according to the predictions discussed in Ref. [24] is expected to be either $\mathrm{De}_d^{-0.5}$ or $\mathrm{De}_d^{-0.75}$.

The lines $f(\mathrm{De}_d)$ depicted in Fig. 3 are quite close to straight ones and have quite similar inclination to the horizontal axis. The exponent a can be estimated using the values of the friction factor f_1 and f_2 at two arbitrary values of the Dean number $\mathrm{De}_{d,1}$ and $\mathrm{De}_{d,2}$ as

$$a = -\frac{\ln(f_1) - \ln(f_2)}{\ln(\mathrm{De}_{d,1}) - \ln(\mathrm{De}_{d,2})}. \tag{8}$$

Calculation by Eq. (8) between two points corresponding to $\mathrm{Re}_d \approx 1000$ and $\mathrm{Re}_d \approx 5000$ for all numerical lines shown in Fig. 3 yielded values close to 0.6, which would mean that the previous result reporting $a = 0.5$ are more accurate. However, monitoring how the exponent a varies between every two consequent points obtained for Fig. 3, we arrive to the dependences shown in Fig. 4. We observe that at very small Reynolds numbers the effect of curvature is weak, so that the exponent a tends to unity (the straight pipe result) when the Reynolds number tends to zero. With the growth

of the Reynolds number from $\mathrm{Re}_d \approx 200$ to $\mathrm{Re}_d \approx 500$ and $\varepsilon < 0.05$, the exponent a steeply decreases and then switches to a much slower decay slightly above the value of $a = 0.6$. At larger supercriticalities the slower decay starts from larger Reynolds number and the exponent attain the values slightly below $a = 0.6$. We arrive to a conclusion that an accurate power dependence of the friction factor on the Dean or Reynolds number does not exist. At the same time between $\mathrm{Re}_d \approx 2000$ and $\mathrm{Re}_d \approx 5000$ the value $a = 0.6$ can be used as a "rule of thumb" for quite wide interval of the curvatures.

B. Stability diagrams

Study of the primary instability of the helical pipe flow was carried out for $0 < \varepsilon \leqslant 0.6$ and $0 \leqslant \lambda \leqslant 5$. The study can be extended to larger curvatures and torsions, however, such values are unusual for most of applications, as well as for most of academic studies. The computations were carried out on a uniform grid of 100×200 nodes. Several characteristic points on the stability diagram reported below were verified with calculations on a uniform 200×400 and finer grids to ensure that the results coincide at least within the two decimal places, i.e., the disagreement between results obtained on the two grids is less than 1%.

The critical points corresponding to transition from steady to oscillatory flow are reported in Fig. 5. Figure 5(a) shows the dependence of the critical Reynolds number on the torsion-to-curvature ratio for all the values of curvature considered. The flows are stable below and to the left of the curves, and are unstable above and to the right of them. The corresponding critical frequencies and critical wave numbers are shown in Figs. 5(b) and 5(c).

The results reported in Fig. 5 need several additional comments. First, as explained above, $\omega_{\mathrm{cr}} < 0$ means that the instability sets in as a traveling wave propagating downstream. It follows from Figs. 5(b) and 5(c) that for $\lambda \leqslant 1$ all the most critical disturbances are downstream propagating waves. Only at larger torsions $\varepsilon > 0.2$, and not at all the curvatures considered, does the instability set in as an upstream propagating wave.

Second, the linearized stability problem is invariant under the replacement $k \rightarrow -k$ and $\omega \rightarrow -\omega$. For each positive value of k_{cr} we found a single eigenvalue with zero real part. No multiple eigenvalues were observed. Also, the real part of leading eigenvalues always crossed the zero axes when the Reynolds number was varied to find the critical point. It allows us to conclude that at calculated critical points $d\sigma/d\mathrm{Re} \neq 0$. Since the wave number k can attain positive and negative values, the whole stability problem has a pair of complex conjugated eigenvalues $(0, \pm\omega_{\mathrm{cr}})$ that correspond to the wave numbers $\pm k_{\mathrm{cr}}$, and their eigenvectors are complex conjugate functions representing the same traveling wave. Thus, we conclude that the steady-oscillatory transition takes place as a Hopf bifurcation [30].

Third, we observe several most unstable modes that replace each other when the curvature and the torsion are varied. These modes are represented by separate lines in Figs. 5(b) and 5(c). A replacement of an unstable mode by another one causes more or less noticeable breaks of the $\mathrm{Re}_{\mathrm{cr}}(\lambda)$ curves shown in Fig. 5(a). Note that an existence of many most unstable modes is quite usual for parametric stability studies (see, e.g., [25] and references therein).

In Figs. 5(b) and 5(c) the different most unstable eigenmodes are numbered according to their appearance in the calculations. The same number is attained to modes with similar eigenvector patterns. A Table I summarizes the curvature values and intervals of λ where all the numbered eigenmodes are observed. The third column contains a short description of the observed features of the corresponding disturbance. The two last columns of the table contain links to animations, in which time dependencies of perturbation patterns and slightly supercritical flows are visualized to help understand the descriptions given in Sec. V 3.

C. Visualization of slightly supercritical flows

Recalling that all the disturbances are proportional to $\exp(ik_{\mathrm{cr}}s + i\omega_{\mathrm{cr}}t)$, we note that for a single-frequency time-periodic flow, oscillations in time at fixed s are similar to oscillations along the
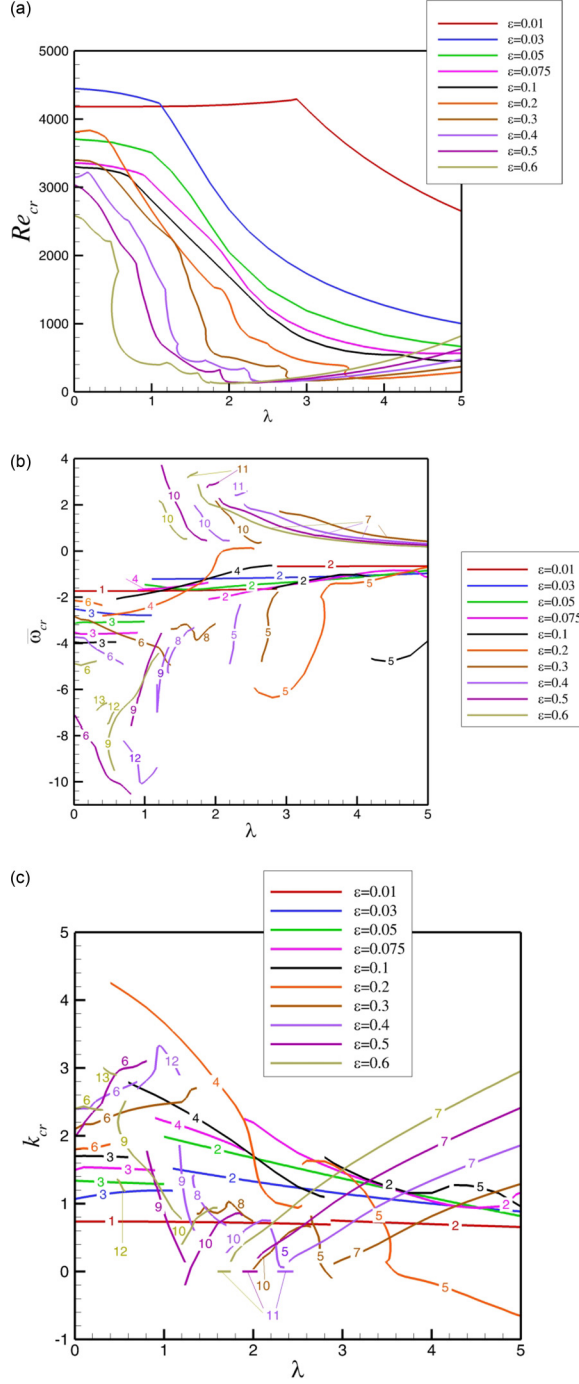
FIG. 5. (a) Critical Reynolds number versus the torsion to curvature ratio at different dimensionless curvatures; (b) critical oscillations frequency versus the torsion to curvature ratio at different dimensionless curvatures; (c) critical wave number versus the torsion to curvature ratio at different dimensionless curvatures.

spatial period $s_0 \leqslant s \leqslant s_0 + 2\pi/k_{cr}$ at fixed time. Therefore, in the following we visualize only oscillations in time at an arbitrary fixed location s.

Each most unstable eigenmode can be plotted as a time-dependent function, or just as its absolute value showing the distribution of the oscillations amplitude. In this section we discuss how oscillations of the Dean vortices, i.e., oscillations of the secondary cross-pipe flow can be visualized. To do this we use the visualization method described in Ref. [26], and calculate a divergence free projection of velocity on the plane (r, ξ). For the base flow, which is independent of s, this projection is given by Eq. (6) and is $\boldsymbol{V}_{2D} = (v_r, v_\xi - \varepsilon\lambda r v_s/H_s, 0)$, div$\boldsymbol{V}_{2D} = 0$. In the toroidal pipe, at $\lambda = 0$, the pseudo-streamfunction becomes the true stream function, so that its isolines are the streamlines in the polar plane (r, ξ). In the helical pipe with a nonzero torsion, the pseudo-streamlines deviate from the spiraling streamlines, however still describe the vortical motion in the cross-flow planes [7,9].

Since there is no analytical expression for the divergence free projection of an arbitrary three-dimensional disturbance, it is calculated by the iterative SIMPLE-like procedure described in Ref. [26]. As a result, the disturbance in the fixed plane $s = s_0$ is expressed as $\tilde{\boldsymbol{v}} = \tilde{\boldsymbol{v}}_{2D} + \nabla\varphi$, where $\tilde{\boldsymbol{v}}_{2D} = (\tilde{v}_{r,2D}, \tilde{v}_{\xi,2D}, 0)$, and $\nabla \cdot \tilde{\boldsymbol{v}}_{2D} = 0$. The vector $\tilde{\boldsymbol{v}}_{2D}$ is the divergence-free projection of the three-dimensional disturbance vector on a plane (r, ξ). It can be represented as $\tilde{\boldsymbol{v}}_{2D} = \text{rot}\,\tilde{\boldsymbol{\psi}}_{2D}$, where the vector potential $\tilde{\boldsymbol{\psi}}_{2D}$ has a form $\tilde{\boldsymbol{\psi}}_{2D} = (0, 0, \tilde{\psi}_{2D})$, so that $\tilde{\psi}_{2D}$ is an analog of a two-dimensional stream function. The difference between the vectors $\tilde{\boldsymbol{v}}$ and $\tilde{\boldsymbol{v}}_{2D}$ can be roughly estimated using the three-dimensional continuity (A8) and is expected to be of the order $k|\tilde{v}_s|$. Now a slightly supercritical oscillatory flow can be visualized using

$$v_s = V_s(r, \xi) + \epsilon\text{Real}[\tilde{v}_s(r, \xi)\exp(ik_{cr}s + i\omega_{cr}t)], \tag{9}$$

$$\Psi = \psi(r, \xi) + \epsilon\text{Real}[\tilde{\psi}_{2D}(r, \xi)\exp(ik_{cr}s + i\omega_{cr}t)], \tag{10}$$

where V_s and $\tilde{v}_s$ are the center line s components of the base flow and the disturbance, respectively, ψ is the pseudo-streamfunction of the base flow defined in Eq. (6), and Ψ is the pseudo-streamfunction of the divergence free projection of the slightly oscillatory flow state. The amplitude ϵ is a function of the super-criticality (Re $-$ Re$_{cr}$), which cannot be found within the linear stability approach. Its finding requires either a nonlinear analysis of bifurcation, or a fully three-dimensional time-dependent solution, both of which are beyond the scope of this study. Here we are interested only in qualitative visualization of patterns of slightly supercritical flows. For this purpose, we choose the value of ϵ so that the amplitude of the second terms of Eqs. (9) and (10) do not exceed 10% of the amplitude of the first terms, while the oscillations of both the center line velocity and the cross-sectional flow are visible.

An example of this visualization is presented in Figs. 6 and 7 and the corresponding animations. Color plots in Fig. 6 show snapshots of the leading perturbation of the three velocity components distanced by a quarter of the time oscillation period. The isolines of the center line velocity and the pseudo-streamfunction of the base flow are shown by lines. This figure shows that the velocities v_s and v_r are perturbed antisymmetrically with respect to the pipe diameter $= 0, \pi$, while the perturbation of v_ξ is symmetric. However, these perturbation patterns are not very helpful in understanding of how the flow changes in a slightly supercritical regime. The answer to this question is presented in Fig. 7, where snapshots of the functions defined in Eqs. (9) and (10) are shown. In this figure and the corresponding animation we observe slight oscillations of the center line velocity, and oscillations of the Dean vortices that oscillate in a counterphase. Below, based on the described visualization of disturbances and slightly supercritical flows, we make an attempt to classify the eigenmodes and to gather some more understanding in the processes leading to the onset of different instability modes. For this purpose all 13 modes observed are presented as animations in the Supplemental Material [27]. The guidance is given in the table there, where all visualized cases are listed. In the figures below we illustrate only most characteristic modes in the same way as it was done in Figs. 6 and 7.
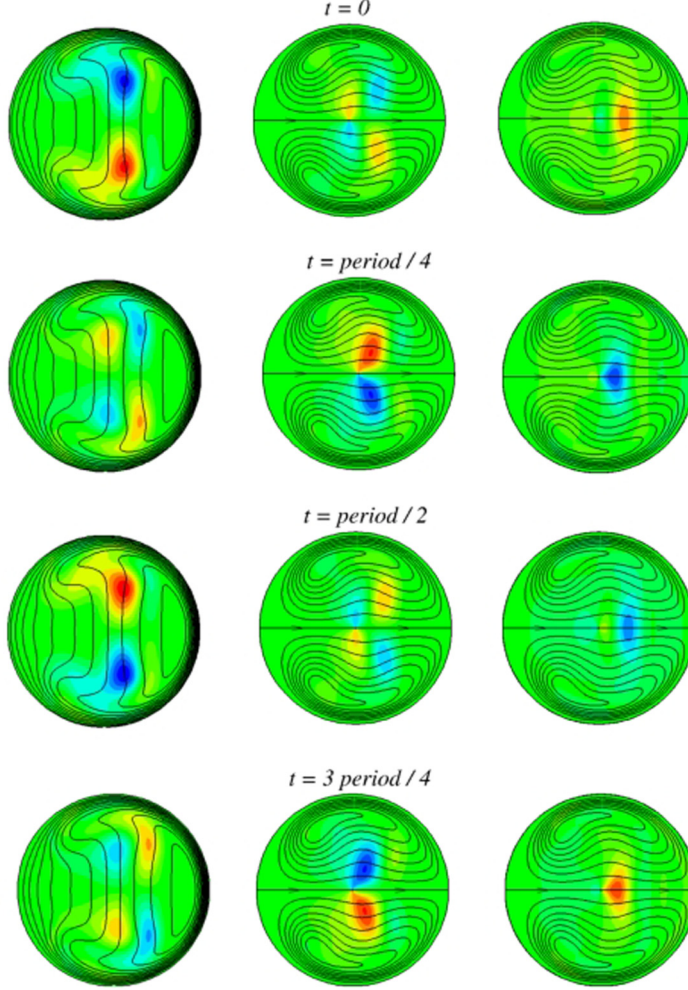
FIG. 6. Oscillations of the most unstable perturbation at $\varepsilon = 0.01$, $\lambda = 0$, $\mathrm{Re}_{cr} = 4181$ (mode 1). Left frames: perturbation of the center line velocity superimposed with isolines of the base flow center line velocity (lines); center and right frames, respectively: perturbations of v_r and v_ξ superimposed with the pseudo-streamlines of base flow (lines). All the levels are equally spaced between the minimal and maximal values. Perturbation: $\max|\tilde{v}_s| = 0.0192$, $\max|\tilde{v}_r| = 0.00561$, $\max|\tilde{v}_\xi| = 0.00795$. Base flow: $\max|v_s| = 1.696$, $\max|\psi| = 0.0101$. Animation files: Perturbation_e=0p01_l=0.avi, Perturbation_e=0p01_l=2.avi.

D. Classification and description of the unstable eigenmodes

In the discussion below we make an attempt to classify the most unstable modes and to discuss which physical mechanisms can be responsible for onset of instabilities and for appearance of self-sustained oscillations of supercritical states. Clearly, such descriptions are mostly qualitative and sometimes even speculative, but nevertheless, we are making an attempt to provide some more insight into this question. First we note that results obtained for instabilities of inviscid vortices [31–33], as well as for inviscid vortex pairs [34–36], in an unbounded domain, cannot be applied to the bounded viscous flow considered here. Moreover, in the present helical pipe configuration, the flow through the pipe and the secondary Dean vortices are already interconnected in the base flow,
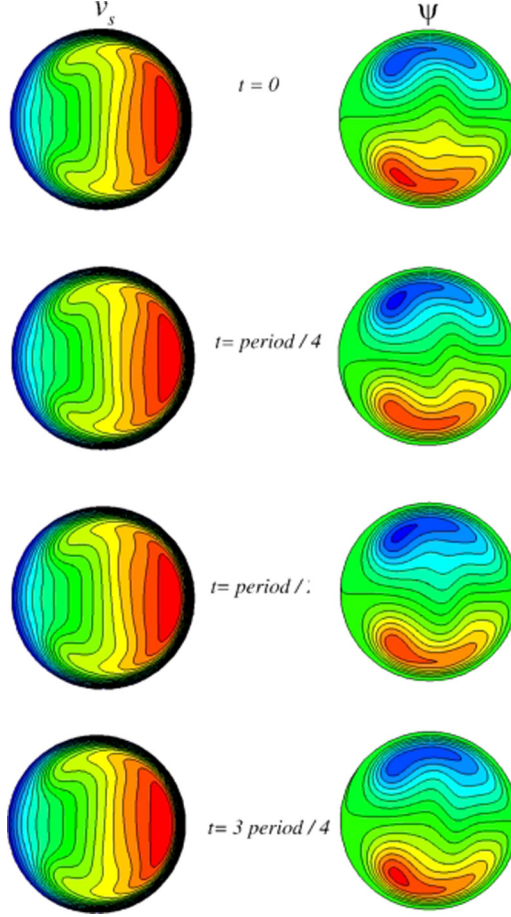
FIG. 7. Snapshots of a slightly supercritical oscillatory flow at at $\varepsilon = 0.01$, $\lambda = 0$, $\mathrm{Re_{cr}} = 4181$. The levels are equally spaced between 0 and 1.6 for v_s and between ± 0.1 for ψ. Animation files: Flow_e=0p01_l=0.avi, Flow_e=0p01_l=2.avi.

contrarily to inviscid vortices superimposed with axial flow (e.g., Ref. [35]) or with background rotation (e.g., Refs. [31,37]).

To examine which terms of the linearized equations contribute or do not contribute to the instability onset, we eliminate them individually and monitor the leading eigenvalue and pattern of the leading eigenvector. This simple computational experiment, successfully applied in Ref. [38] and later studies, allows us to focus only on the terms responsible for the disturbances growth and to avoid discussing the irrelevant ones. In the text below we call it "zeroing terms numerical experiment."

1. Critical modes at zero torsion

We start from the limiting case of zero torsion, $\tau = \lambda = 0$, which corresponds to a toroidal pipe [6,18]. In this case the isolines of the center line velocity are always symmetric with respect to the diameter line $= 0, \pi$, while the Dean vortices are always antisymmetric (Figs. 5–11). The s component of flow vorticity and the pseudo-streamfunction ψ are also antisymmetric, so that, e.g., $\psi(\xi) = -\psi(2\pi - \xi)$. The instability can break this symmetry or preserve it, which allows us to
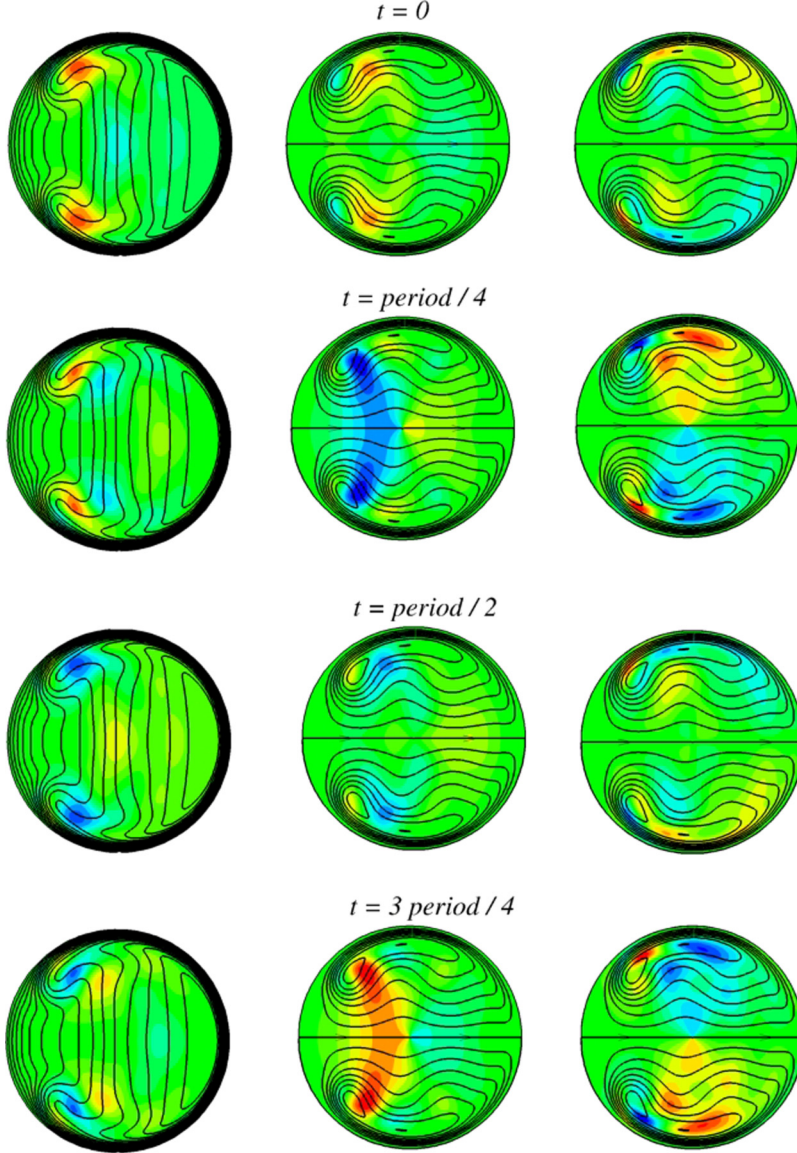
FIG. 8. Oscillations of the most unstable perturbation at $\varepsilon = 0.075$, $\lambda = 0$, $\mathrm{Re_{cr}} = 3357$ (mode 3). Left frames: perturbation of the center line velocity superimposed with isolines of the base flow center line velocity (lines); center and right frames, respectively: perturbations of v_r and v_ξ superimposed with the pseudo-streamlines of base flow (lines). All the levels are equally spaced between the minimal and maximal values. Perturbation: $\max|\tilde{v}_s| = 0.0245$, $\max|\tilde{v}_r| = 0.0646$, $\max|\tilde{v}_\xi| = 0.00567$. Base flow: $\max|v_s| = 1.619$, $\max|\psi| = 0.0195$. Animation file: Perturbation_e=0p075_l=0.avi.

make the first distinction between the eigenmodes. With the increasing curvature, these symmetric flows become unstable owing to the three modes 1, 3, and 6, described below.

At very small curvatures the instability breaks the symmetry, as is seen from Fig. 7 plotted for $\varepsilon = 0.01$, $\lambda = 0$. This instability mode is denoted as mode 1. Note that the perturbations $\tilde{v}_s$ and $\tilde{v}_r$ are antisymmetric and break the symmetry of the corresponding symmetric components v_s and v_r
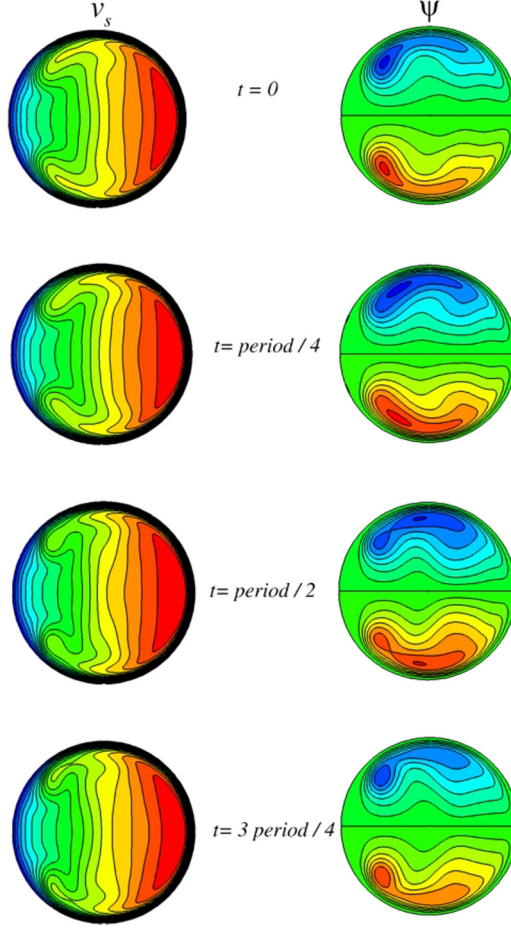
FIG. 9. Snapshots of a slightly supercritical oscillatory flow at $\varepsilon = 0.075$, $\lambda = 0$, $\mathrm{Re_{cr}} = 3357$. The levels are equally spaced between 0 and 1.5 for v_s and between ± 0.02 for ψ. Animation file: Flow_e=0p075_l=0.avi.

of the base flow (Fig. 6). The base flow component v_ξ is antisymmetric, while its perturbation is symmetric and breaks its antisymmetry.

The above mentioned interconnection between the primary center line and the secondary Dean vortex flow helps to understand the oscillatory mechanism of mode 1 (Figs. 6 and 7). We note first that the through flow loses energy both owing to viscosity and to work of centrifugal and Coriolis forces, which produce the Dean vortices. An increase in the center line velocity caused by a positive value of perturbation in the lower part of the upper left frame of Fig. 6 (the first period quarter) increases the centrifugal force, which leads to an intensification of the positive clockwise Dean vortex in the right frame of the first period quarter in Fig. 7. As a result, the zero pseudo-streamline is deformed inwards to the negative vortex, so that the positive vortex occupies a slightly larger volume than the negative one. The intensification of the positive vortex causes larger energy losses by the through flow in the part of the flow region it occupies, which slows down the through flow there. The latter is observed at the third quarter of the oscillation period (Fig. 6), where perturbation of the center line velocity in the lower part becomes negative, while attaining a large positive value in the upper part. This leads to the intensification of the negative vortex, followed by decrease of the center line velocity in the corresponding part of the flow region. Finally, the oscillations of both vortices and of the center line velocity become self-sustained.
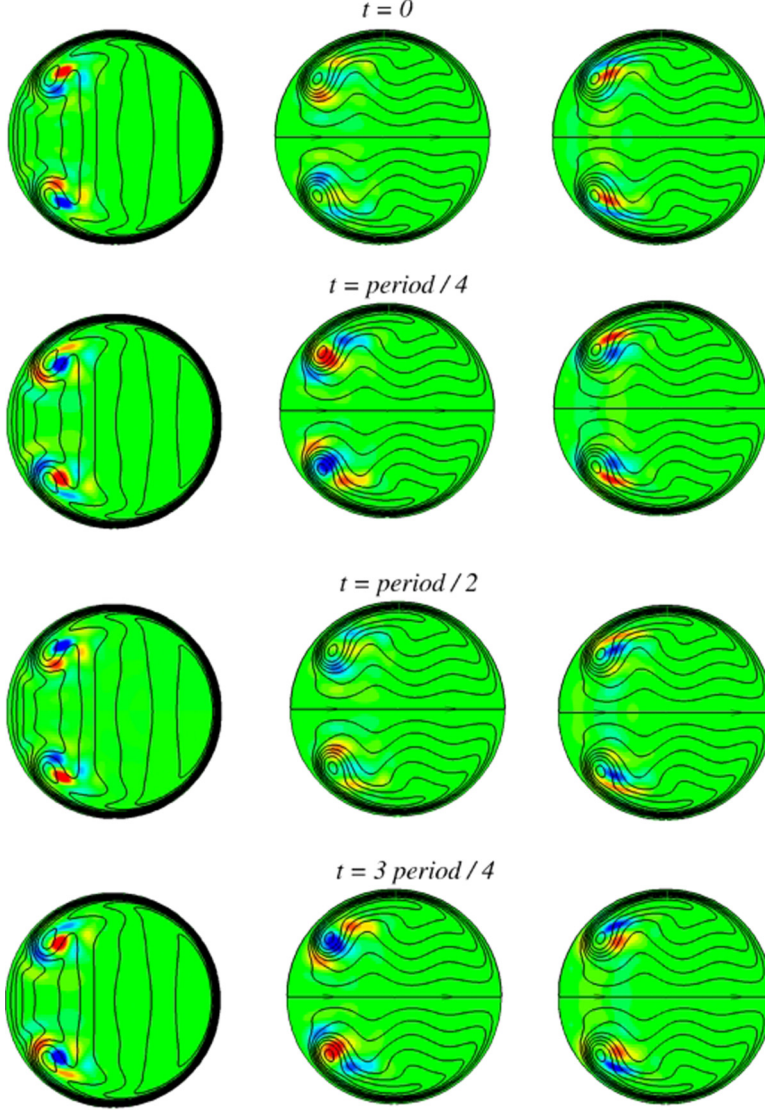
FIG. 10. Oscillations of the most unstable perturbation at $\varepsilon = 0.2$, $\lambda = 0$, $\mathrm{Re_{cr}} = 3802$ (mode 6). Left frames: perturbation of the center line velocity superimposed with isolines of the base flow center line velocity (lines); center and right frames, respectively: perturbations of v_r and v_ξ superimposed with the pseudo-streamlines of base flow (lines). All the levels are equally spaced between the minimal and maximal values. Perturbation: $\max|\tilde{v}_s| = 0.0531$, $\max|\tilde{v}_r| = 0.0167$, $\max|\tilde{v}_\xi| = 0.0232$. Base flow: $\max|v_s| = 1.511$, $\max|\psi| = 0.0260$. Animation files: Perturbation_e=0p2_l=0.avi, Perturbation_e=0p3_l=0.avi, Perturbation_e=0p4_l=0.avi, Perturbation_e=0p5_l=0.avi, Perturbation_e=0p6_l=0.avi.

The zeroing terms numerical experiment, performed for the parameters of Figs. 6 and 7, shows that to obtain a similar eigenvalue and eigenvector one can leave in the perturbed momentum equations (A4)–(A6) the terms $ikV_s\tilde{\boldsymbol{u}}/H_s$, $[2V_\xi\tilde{u}_\xi/r + 2\varepsilon\sin(\xi)V_s\tilde{u}_s/H_s]\boldsymbol{e}_r$, $2\varepsilon\cos(\xi)V_s\tilde{u}_s\boldsymbol{e}_\xi/H_s$, and $\frac{\varepsilon}{H_s}V_s[\tilde{u}_\xi\cos(\xi) + \tilde{u}_r\sin(\xi)]\boldsymbol{e}_s$, and to zero all the others. The first vector term shows that advection of disturbances of all the three velocity components along the pipe center line is necessary for the instability onset. The next two terms show that perturbation of the center line velocity u_s affects
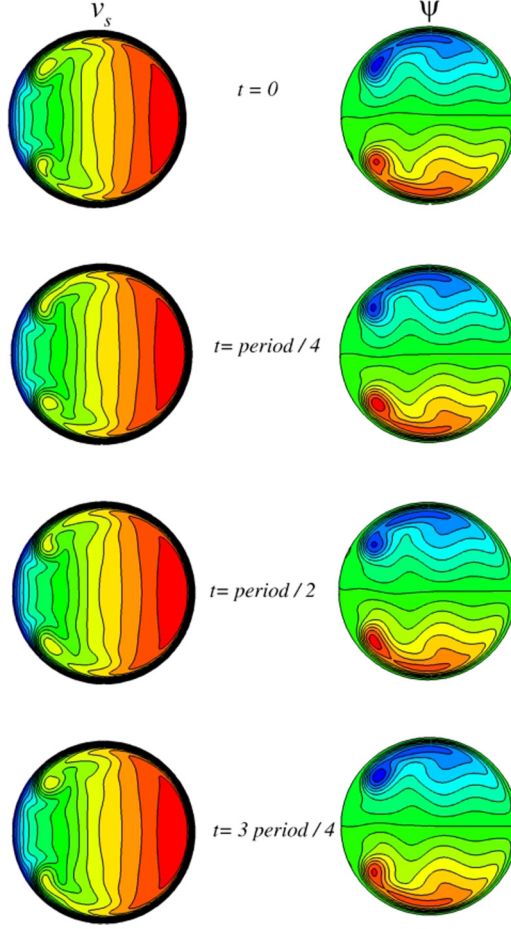
FIG. 11. Snapshots of a slightly supercritical oscillatory flow at $\varepsilon = 0.2$, $\lambda = 0$, $\mathrm{Re}_{cr} = 3802$. The levels are equally spaced between 0 and 1.4 for v_s and between ± 0.025 for ψ. Animation file: Flow_e=0p2_l=0.avi.

the radial and circumferential velocities via the centrifugal and Coriolis forcing. An additional centrifugal forcing comes from the circumferential velocity perturbation. The last term is the Coriolis forcing responsible for affecting the center line velocity perturbation by two other perturbed components.

Unfortunately, considering other instability modes, we cannot point to a similar simple mechanism of self-sustained oscillations.

At $\varepsilon = 0.02$, $\lambda = 0$ the instability mode 1 is replaced by another one preserving the symmetry that persists until $\varepsilon = 0.1$. This symmetry preserving instability, denoted as mode 3, is illustrated in Figs. 8 and 9. Contrary to the previous case, the perturbations $\tilde{v}_s$ and $\tilde{v}_r$ are symmetric, while the perturbation $\tilde{v}_\xi$ is antisymmetric (Fig. 8). The Dean vortices oscillate in phase (Fig. 9), so that the zero pseudo-streamline separating the vortices remains nondeformed. It is easy to verify that when the center line velocity increases, the intensity of vortices, measured by the maximal and minimal values of the pseudo-streamfunction, decreases and vice versa. This rules out the oscillations mechanism described above, where increase of center line velocity and intensification of the Dean vortices takes place simultaneously. More likely, we observe here an exchange of energy between the through flow and the Dean vortices. Another qualitative difference in both cases can be seen by comparing the snapshots of the oscillatory flow (cf. Figs. 7 and 9, and corresponding animations).

In the case of mode 1 (Fig. 7), the zero pseudo-streamline oscillates, and an intensification of one vortex is followed by a weakening of the second one, so that the vortices affect each other. In the case of mode 3, the zero pseudo-streamline at $\lambda = 0$ (Fig. 9) remains nondeformed, and the vortices grow and diminish simultaneously, so that no interaction between the vortices is observed.

Several additional numerical experiments showed that if the terms $\tilde{u}_r \frac{\partial V_r}{\partial r} \boldsymbol{e}_r$, $\frac{\tilde{u}_r}{r} \frac{\partial (rV_\xi)}{\partial r} \boldsymbol{e}_\xi$, and $(V_r \frac{\partial \tilde{u}_s}{\partial r} + \frac{V_\xi}{r} \frac{\partial \tilde{u}_s}{\partial \xi}) \boldsymbol{e}_s$ are set to zero, then the eigenvalue and the eigenvector remain close to those computed via the full equations. The unimportance of the last term shows that advection of the center line velocity perturbation along the base flow Dean vortices does not affect the instability. The unimportance of the first two terms means that advection of the mean flow V_r and V_ξ components along the r direction does not affect the instability, while this is not true regarding the ξ direction. Advection in the s direction of all the flow components, base and perturbed, remains important. This brings us to the problem of the stability of a pair of vortices superimposed on a through flow [35,39]. However, as it was already mentioned, in the considered problem the vortices and the through flow are interconnected, and the flow is viscous, which makes the results obtained in the above studies inapplicable. Thus, the perturbation patterns reported in Ref. [35] are qualitatively different from those depicted in Fig. 8, as well as from all the others perturbation patterns reported below.

Continuing discussion and description of mode 3, we notice that the base flow component V_ξ, changing between ± 0.12, is noticeably larger than V_r changing between -0.04 and $+0.02$, so that advection along the ξ direction is expected to be dominant. Also, the maximal and minimal values of the perturbation u_s are located in the areas where the isolines of the center line velocity V_s are strongly curved (Fig. 8). One-dimensional profiles of V_s in this region have inflection points, which indicates on a possibility of an inviscid instability mechanism. Obviously, this criterion remains only an indication and cannot be applied for the considered flow.

Another possibility follows from relatively large values of V_ξ and the localization of the perturbation u_ξ near the upper and lower borders (rightmost frames in Fig 8). The isolines of V_ξ, not shown in above figures, exhibit a boundary layer near these parts of the border. Some characteristic profiles $V_\xi(r)$ plotted via the point where the base circumferential velocity attains its maximum are shown in Fig. 12 for this and other modes, where a developed boundary layer of V_ξ was observed, so that the circumferential velocity steeply grows from the boundary point inside the pipe. Thus, in the case of mode 3, and other cases when the perturbation u_ξ is localized near or inside the boundary layer of V_ξ, we can assume a boundary layer instability that also may interact with other destabilizing flow features.

Starting from $\varepsilon = 0.2$ and keeping $\lambda = 0$, we observe the symmetry breaking instability again, however it leads to a qualitatively different pattern of the slightly supercritical flow (Figs. 10 and 11 and the corresponding animations). This disturbance mode is denoted as mode 6. The perturbations of all the velocity components are localized near the Dean vortices "centers," where the pseudo-streamfunction attains the minimal and maximal values. Oscillations of the Dean vortices are noticeable only near their "centers," while far from there the vortices remain almost steady. Examining the corresponding animations, listed in the Supplemental Material [27], we observe that the perturbations are advected along the pseudo-streamlines from the regions of relatively large cross-flow velocities, where the streamlines are close, to the regions where the pseudo-streamfunction attain its largest and smallest values, so that the cross flow velocities there are small due to the small derivatives $\partial \psi / \partial r$ and $\partial \psi / \partial \xi$. In these regions the disturbances fully dissipate. This mode of instability persists in the toroidal pipe ($\lambda = 0$) up to $\varepsilon = 0.6$.

The above observations of the leading perturbation patterns characteristic for the symmetric flows in the toroidal pipe, allow us to introduce some features that will help us to classify disturbances of nonsymmetric flows at nonzero torsion. Thus, we can distinguish them by weak or strong oscillations of the zero pseudo-streamline separating two Dean vortices, where strong oscillations will correspond to the symmetry breaking mode 1, while weak oscillations will be compared either with the symmetry preserving mode 3 or the symmetry breaking mode 6. We can examine whether the Dean vortices oscillate in close phases, similar to the symmetry preserving mode, or
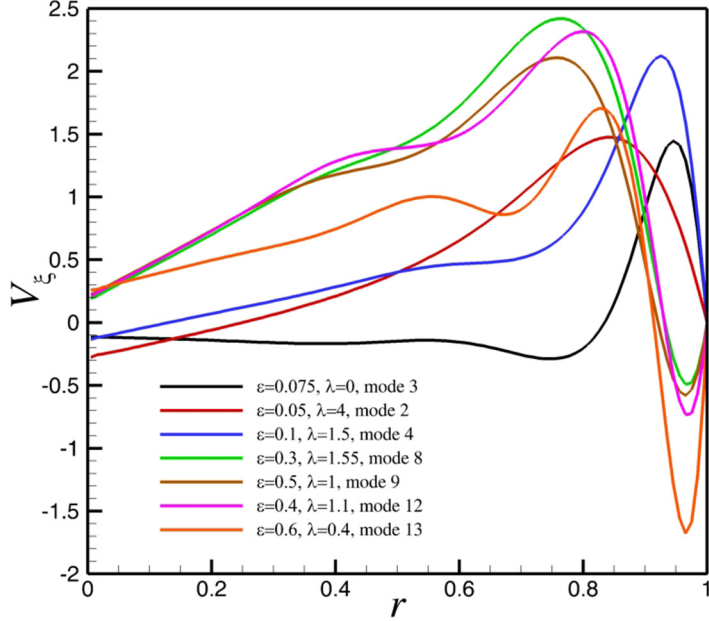
FIG. 12. Radial profiles of the base flow circumferential velocity passing through its maximum located inside the clockwise Dean vortex (modes 2, 3, 4, 9) or the minimum located in the counterclockwise Dean vortex (modes 10, 13, 14).

at noticeably different phases, similarly to the symmetry breaking modes. The perturbations can be characterized by their distribution over the whole bulk of the vortices or localization in certain flow regions.

Thus, quite expected changes of the perturbations and slightly supercritical flows are observed along the parts of neutral curves corresponding to modes 1 and 3 (not shown in the figures, only in the animations; see the Supplemental Material [27]). For example, at $\varepsilon = 0.01$, $\lambda = 2$ the Dean vortices oscillate in counterphases and are similar to those depicted in Fig. 7. At $\varepsilon = 0.03$, $\lambda = 1$, the vortices oscillations are in close phases and are similar to those shown in Fig. 9.

2. Instabilities growing in the stronger counterclockwise negative vortex

Examining mode 6 at larger curvatures one observes that the supercritical flow changes qualitatively along the same eigenmode branch. This is seen in the animations of mode 6 for $\varepsilon \geqslant 0.3$. With the increase of torsion, the negative vortex becomes more intensive than the positive one. As a result, the instability sets in only inside the stronger negative vortex, located in the upper part of the pseudo-streamlines plot. The flow oscillations are seen only inside the stronger negative vortex, while the positive vortex remains almost unchanged along the oscillation period. This leads us to a conclusion that interaction of the two Dean vortices play no role in the onset of this mode of instability. Since the perturbations attain their largest values far from the boundaries, we cannot assume here a boundary layer instability. At the same time, we observe again an inflection point at the $V_s(r)$ profile that passes through the minimum of the pseudo-streamfunction, in the neighborhood of which we observe large perturbations of all the three velocity components. Thus, we can assume here an inviscid instability of the through flow, which appears in both vortices in the antisymmetric configuration, and only in a stronger counterclockwise vortex in a nonsymmetric case (see corresponding animations listed in the table in the Supplemental Material [27]).

Mode 8 develops in a stronger counterclockwise vortex (Figs. 13 and 14) and is observed at $\varepsilon = 0.3$, $1.37 \leqslant \lambda \leqslant 2$, and $\varepsilon = 0.4$, $1.33 \leqslant \lambda \leqslant 1.7$. In this case the torsion is moderate, so that
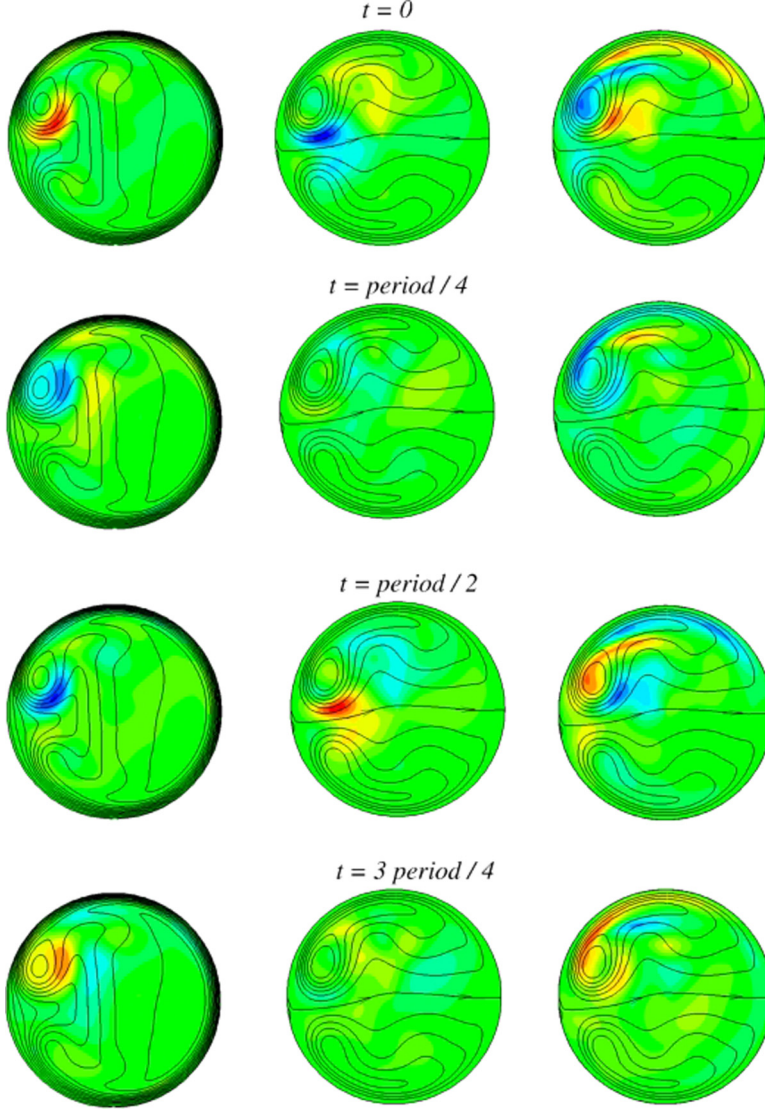
FIG. 13. Oscillations of the most unstable perturbation at $\varepsilon = 0.3$, $\lambda = 1.55$, $\mathrm{Re}_{cr} = 1384$ (mode 8). Left frames: perturbation of the center line velocity superimposed with isolines of the base flow center line velocity (lines); center and right frames, respectively: perturbations of v_r and v_ξ superimposed with the pseudo-streamlines of base flow (lines). All the levels are equally spaced between the minimal and maximal values. Perturbation: $\max|\tilde{v}_s| = 0.0299$, $\max|\tilde{v}_r| = 0.0124$, $\max|\tilde{v}_\xi| = 0.0136$ Base flow: $\max|v_s| = 1.375$, $\psi_{\min} = -0.0711$, $\psi_{\max} = 0.0475$. Animation files: Perturbation_e=0p3_l=1p55.avi.

both the clockwise and counterclockwise vortices of the base flow are well developed, while the counterclockwise vortex is slightly stronger (Fig. 13). The structures of mode 8 are noticeably larger than those of mode 6. Oscillations of this disturbance mode are seen in almost all bulk of the counterrotating vortex, however, as is seen from the animations, they cannot be characterized as an azimuthal traveling wave. Contrary to mode 6, we observe penetration of the perturbations $\tilde{v}_s$ and $\tilde{v}_r$ into the weaker clockwise vortex, which results in quite visible oscillations of the clockwise vortex and the zero pseudo-streamline (Fig. 14 and the corresponding animation).
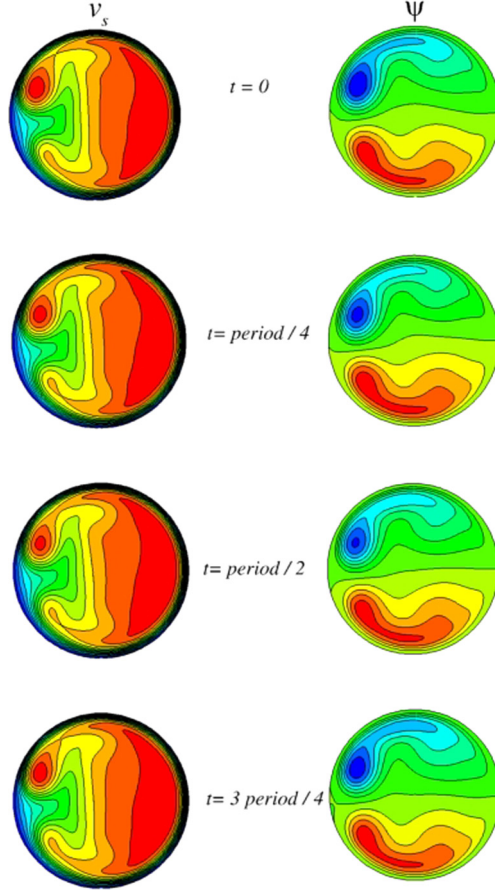
FIG. 14. Snapshots of a slightly supercritical oscillatory flow at $= 0.3$, $\lambda = 1.55$, $\mathrm{Re_{cr}} = 1384$. The levels are equally spaced between 0 and 1.3 for v_s and between -0.06 and 0.04 for ψ. Animation files: Flow_e=0p3_l=1p55.avi.

Neglecting of each term of the linearized equations leads to a noticeable change of the disturbances pattern or the eigenvalue. To estimate relative intensity of the Dean vortices of the flow shown in Fig. 13, we note that the minimum and maximum of the pseudo-streamfunction are approximately -0.071 and 0.047. The minimal value of the circumferential velocity in the stronger counterclockwise vortex is ≈ -0.1, while in the weaker clockwise vortex the maximal value is ≈ 0.68. Nevertheless, the instability sets in the counterclockwise vortex, but not in a weaker clockwise one, as one could expect. Also, contrary to several examples below, we do not observe here clear advection of the disturbances along or against the Dean vortices. An indication on a possible instability mechanism is revealed from the radial profile of V_ξ plotted through a point of its minimum located near the upper pipe border, also shown in Fig. 12. Here we observe that the circumferential velocity magnitude grows from the zero value at the wall to the minimum of V_ξ. Then the circumferential velocity steeply increases to, even larger in magnitude, positive maximal value. Furthermore, changing the sign, the profile exhibits a clear inflection point, so that we observe a configuration of the local mixing layer. The viscous mixing layer becomes unstable at rather small Reynolds numbers [40], so that this locally developing mixing layer configuration can be a source of the instability.

Mode 9 appears in narrow intervals of λ at $0.4 \leqslant \varepsilon \leqslant 0.6$ as an upstream wave developing on the stronger counterclockwise vortex (see animations listed in the table in the Supplemental Material [27]). This mode has smaller perturbation structures that can be interpreted as a smaller pseudo-streamlines-wise wave number, and almost does not penetrate into the weaker vortex. The smaller perturbation structures can be explained by a slightly steeper increase or decrease of the circumferential velocity starting from the boundary (Fig. 12). We observe also that, unlike mode 8, the disturbance structures propagate upstream the dominant counterclockwise Dean vortex. For the flow at $\varepsilon = 0.5$, $\lambda = 1$, the minimal and maximal values of the stream function are -0.86 and 0.67, while the minimal and maximal values of the circumferential velocity are -0.15 and 0.88, where the minimal value is located inside the unstable dominant vortex and the maximal value inside the weaker clockwise vortex. Since the circumferential velocity in the unperturbed clockwise vortex is significantly larger, we cannot connect the instability with the boundary layer of V_ξ. Taking into account that the radial profile plotted through a point of minimum of V_ξ located near the upper pipe border is similar to the previous case (Fig. 12) and also contains the inflection point, we assume again that the instability sets in due to an unstable local mixing layer flow. The zeroing terms numerical experiment shows that we can neglect the terms proportional to the torsion $\varepsilon\lambda$, but not to the curvature itself. Thus, this instability is affected by the centrifugal forcing resulting from the pipe bending, which also shows that the disturbances of all the three velocity components interact on the route to instability onset.

In mode 12, observed only for $\varepsilon = 0.4$ and 0.6 and illustrated in Figs. 15 and 16, we again observe an upstream cross flow wave with a relatively large cross flow wave number developing on the stronger counterclockwise vortex. This mode corresponds to relatively small and moderate torsions, so that both clockwise and counterclockwise Dean vortices remain well developed, and as in the previous cases, the instability arises in the stronger counterclockwise vortex (Fig. 15). The resulting slightly supercritical flow (Fig. 16) exhibits only oscillations of the counterclockwise vortex, while the clockwise one remains almost stationary (see animations listed in the table in the Supplemental Material [27]).

Mode 13, observed only for $\varepsilon = 0.4$ and shown only in animations, exhibits two downstream cross flow waves developing along both Dean vortices. The wave arising along the stronger counterclockwise vortex has a noticeably larger amplitude; however, oscillations of both vortices are clearly seen in the slightly supercritical oscillatory regime.

The $V_\xi(r)$ profiles of modes 12 and 13 also exhibit inflection points near the upper pipe border, and in the case of mode 13 also near the lower border (Fig. 12). Therefore, also in these two cases we assume that the locally developing mixing layer leads to the flow destabilization. Similarly to other flows at large curvatures, we could not find any term of the linearized equations that could be neglected without a qualitative changes in the perturbation patterns. We observe again here that a steeper growth of the circumferential velocity from the pipe wall towards its center, characteristic for mode 13, leads to formation of smaller scale structures in the disturbance patterns, which indicate also on a possible role of the boundary layer instabilities. It is possible also that the two, boundary layer and mixing layer instabilities interact, which results in a self-sustained oscillatory mechanism, yet to be studied and described.

3. Instabilities growing in the weaker clockwise negative vortex

The instability sets in inside a weaker clockwise vortex in the cases of modes 2 and 4. Mode 2 becomes most unstable at small curvatures $\varepsilon \leqslant 0.1$ and relatively large λ. This mode is illustrated in Figs. 17 and 18 for $\varepsilon = 0.05$, $\lambda = 4$. We observe that the most unstable disturbance is located mainly in the clockwise, positive and weaker vortex, and almost does not penetrate in the counterclockwise and stronger one (Fig. 17 and the corresponding animations). As a result, the oscillations of the slightly supercritical flow are visible in the lower part of the snapshots shown in Fig. 18 (see also the corresponding animations), while the upper parts remain almost unchanged. Oscillations of the weaker vortex cause also noticeable oscillations of the zero pseudo-streamline.
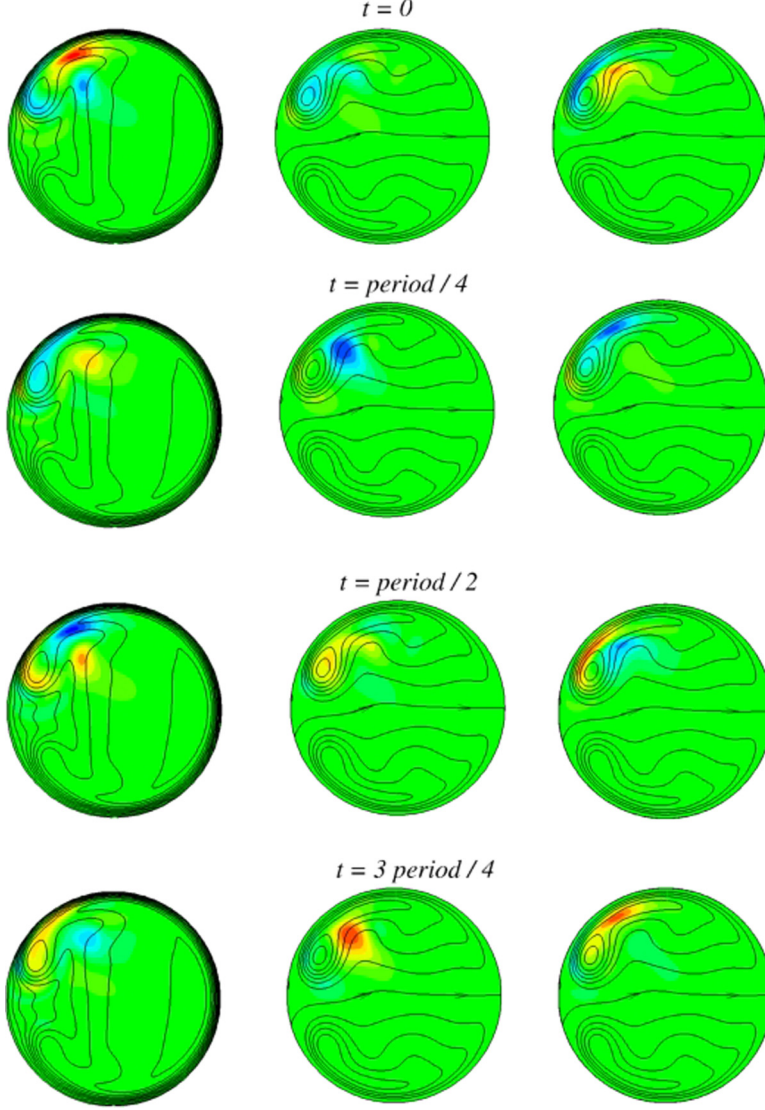
FIG. 15. Oscillations of the most unstable perturbation at $\varepsilon = 0.4$, $\lambda = 1.1$, $\mathrm{Re}_{cr} = 1658$ (mode 12). Left frames: perturbation of the center line velocity superimposed with isolines of the base flow center line velocity (lines); center and right frames, respectively: perturbations of v_r and v_ξ superimposed with the pseudo-streamlines of base flow (lines). All the levels are equally spaced between the minimal and maximal values. Perturbation: $\max|\tilde{v}_s| = 0.0267$, $\max|\tilde{v}_r| = 0.0241$, $\max|\tilde{v}_\xi| = 0.0394$ Base flow: $\max|v_s| = 1.357$, $\psi_{\min} = -0.0646$, $\psi_{\max} = 0.0491$. Animation files: Perturbation_e=0p4_l=1p1.avi, Perturbation_e=0p6_l=0p5.avi.

The zeroing terms numerical experiment carried out for the parameters of Figs. 17 and 18 showed that this instability can be reproduced after neglecting most of bilinear terms. The most interesting is that in Eq. (A6), governing disturbance of the circumferential velocity, we have to leave only the term $-ikV_s\tilde{u}_\xi$ and all the terms containing V_ξ. A closer examination of the perturbation snapshots (Fig. 17) and the corresponding animation reveals that along the path of the disturbance wave propagation, the perturbations of $\tilde{u}_\xi$ appear slightly earlier than the two others. Assuming now that the circumferential motion is a source of instability, we look at the isolines of V_ξ, where we observe
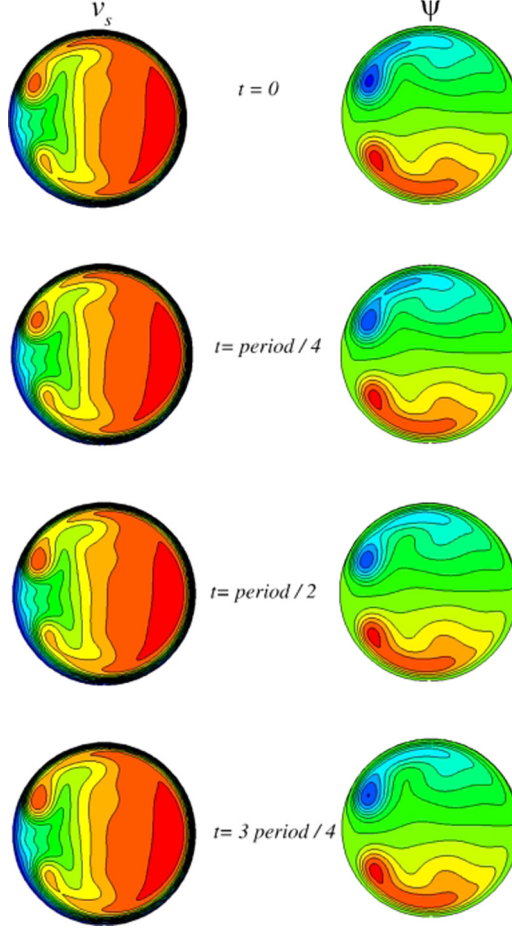
FIG. 16. Snapshots of a slightly supercritical oscillatory flow at $= 0.4$, $\lambda = 1.1$, $\mathrm{Re}_{\mathrm{cr}} = 1658$. The levels are equally spaced between 0 and 1.3 for v_s and between -0.065 and 0.045 for ψ. Animation files: Flow_e=0p4_l=1p1.avi, Flow_e=0p6_l=0p5.avi.

boundary layers that possibly can be unstable. Surprisingly, the largest value of V_ξ in the clockwise Dean vortex is 0.28, while its smallest value in the more intensive counterclockwise vortex is -0.067. Thus, in the lower clockwise vortex the circumferential velocity reaches about a four times larger value, which can explain why the instability sets in inside this vortex only. The radial profile of V_ξ plotted for the value of ξ, corresponding to the location of the maximum of V_ξ near the lower boundary, is shown in Fig. 12 and exhibits a steep increase of the circumferential velocity magnitude from the pipe wall inwards. It should be stressed that the advection along the pipe center line still cannot be neglected. Therefore we observe here an instability of swirling motion, but not of some locally rotational flow.

Another example for disturbance located inside the weaker vortex is shown in Figs. 19 and 20. This perturbation mode, denoted as mode 4, replaces the symmetric mode 3 for $0.05 \leqslant \varepsilon \leqslant 0.2$ [Figs. 5(b) and 5(c)], and is located inside the weaker clockwise lower vortex. Similarly to mode 2, it arises in the regions of large cross flow velocities that are located now close to the pipe border, where boundary layers form at large curvatures and Reynolds numbers. Compared to mode 2, this mode forms noticeably smaller structures around its maximal and minimal values, which are advected along the pseudo-streamlines (Fig. 19). Note, that the stronger counter-clockwise vortex
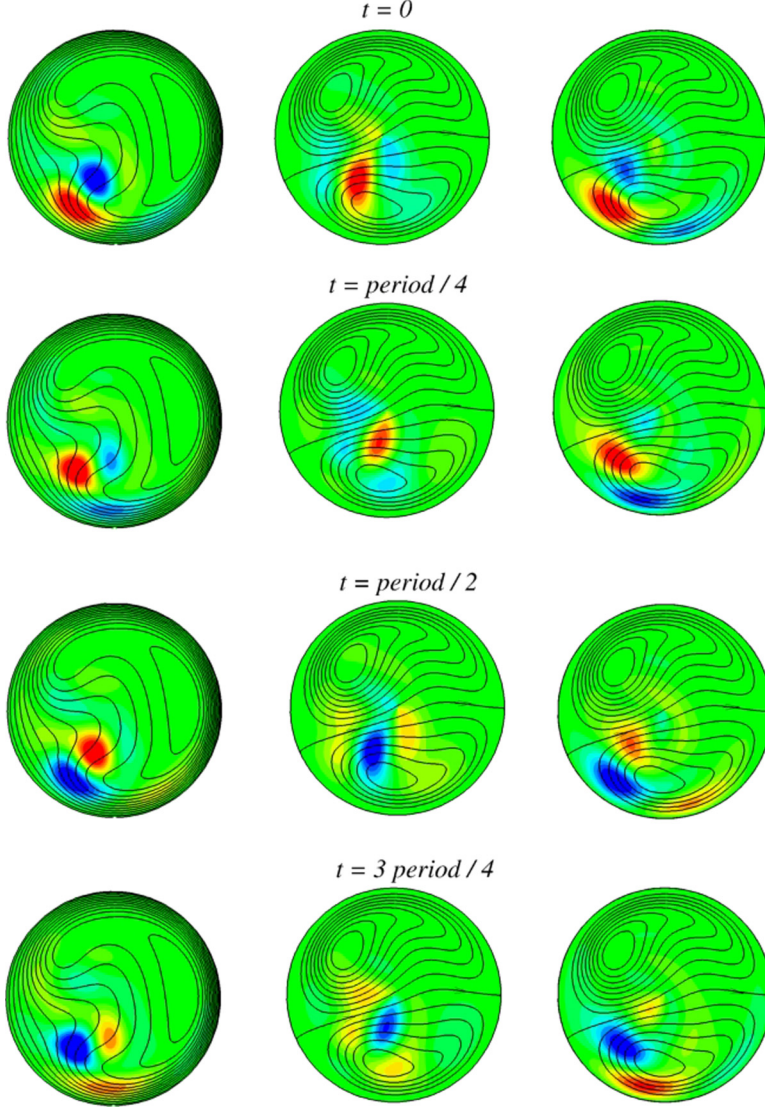
FIG. 17. Oscillations of the most unstable perturbation at $\varepsilon = 0.05$, $\lambda = 4$, $\mathrm{Re_{cr}} = 837$ (mode 2). Left frames: perturbation of the center line velocity superimposed with isolines of the base flow center line velocity (lines); center and right frames, respectively: perturbations of v_r and v_ξ superimposed with the pseudo-streamlines of base flow (lines). All the levels are equally spaced between the minimal and maximal values. Perturbation: $\max|\tilde{v}_s| = 0.0268$, $\max|\tilde{v}_r| = 0.00724$, $\max|\tilde{v}_\xi| = 0.0101$. Base flow: $\max|v_s| = 1.610$, $\psi_{\min} = -0.0451$, $\psi_{\max} = 0.0286$. Animation files: Perturbation_e=0p05_l=4.avi, Perturbation_e=0p05_l=4.avi, Perturbation_e=0p1_l=3.5.avi.

is almost not disturbed and its oscillations are very weak compared to oscillations of the clockwise vortex and the zero pseudo-streamline (Fig. 20 and the corresponding animation). This mode can be characterized as a small circumferential wave number downstream wave.

Assuming that mode 4 triggers the instability inside the boundary layer formed by the circumferential velocity, we notice again that the minimal value of the circumferential velocity in the stronger counterclockwise vortex is ≈ -0.13, while the maximal value in the weaker clockwise
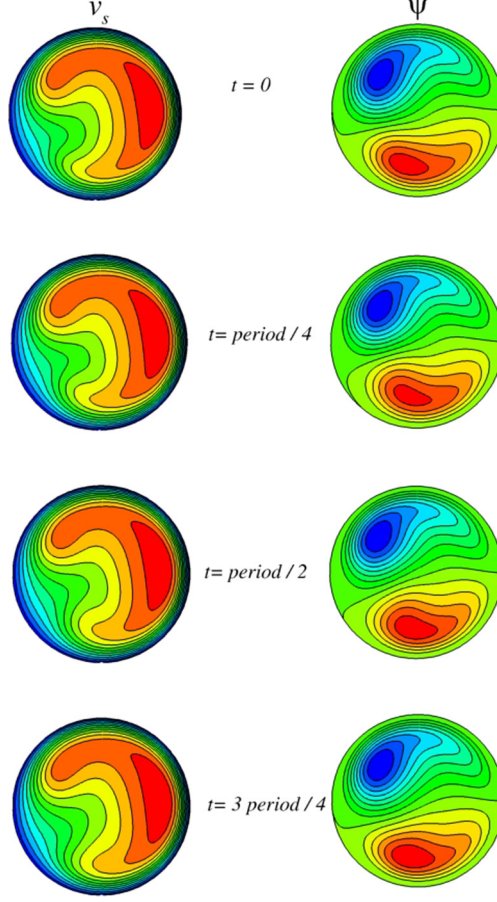
FIG. 18. Snapshots of a slightly supercritical oscillatory flow at $\varepsilon = 0.05$, $\lambda = 4$, $\mathrm{Re_{cr}} = 837$. The levels are equally spaced between 0 and 1.5 for v_s and between -0.040 and 0.025 for ψ. Animation files: Flow_e=0p05_l=4.avi, Flow_e=0p05_l=4.avi, Flow_e=0p1_l=3.5.avi.

vortex is 0.51. Then we examine the radial profile of V_ξ passing through the maximum of V_ξ located near the lower border (Fig. 12). We observe that in the current case the circumferential velocity grows steeper and reaches a smaller minimum value, which can be a reason for smaller-scale wavy structures. The zeroing terms numerical experiment shows that bilinear terms proportional to the dimensionless torsion $\varepsilon\lambda$ play no role in the instability onset. To keep the leading eigenvalue and eigenvector almost unchanged we also can neglect the terms $(u_r \frac{\partial V_r}{\partial r} + \frac{u_\xi}{r} \frac{\partial V_r}{\partial \xi})\boldsymbol{e}_r$ and $\frac{u_\xi}{r} \frac{\partial V_\xi}{\partial \xi} \boldsymbol{e}_\xi$. This means that among all the terms describing advection of the base flow velocities V_r and V_ξ by their disturbances, only advection of V_ξ in the radial direction contributes to the instability onset.

4. Instabilities growing in a dominant or single counterclockwise negative vortex at large torsions

At large torsions the counterclockwise vortex becomes dominating and with the further growth of torsion suppresses the clockwise vortex completely [7,9]. It is not surprising, then, that the instability in these flow sets in owing to qualitatively different most unstable disturbances. Thus, following the neutral curve of $\varepsilon = 0.2$, we arrive to mode 5 illustrated in Figs. 21 and 22. This mode appears at relatively large torsions (see the table in the Supplemental Material [27]), at which the counterclockwise vortex becomes dominant, while the clockwise one is either noticeably
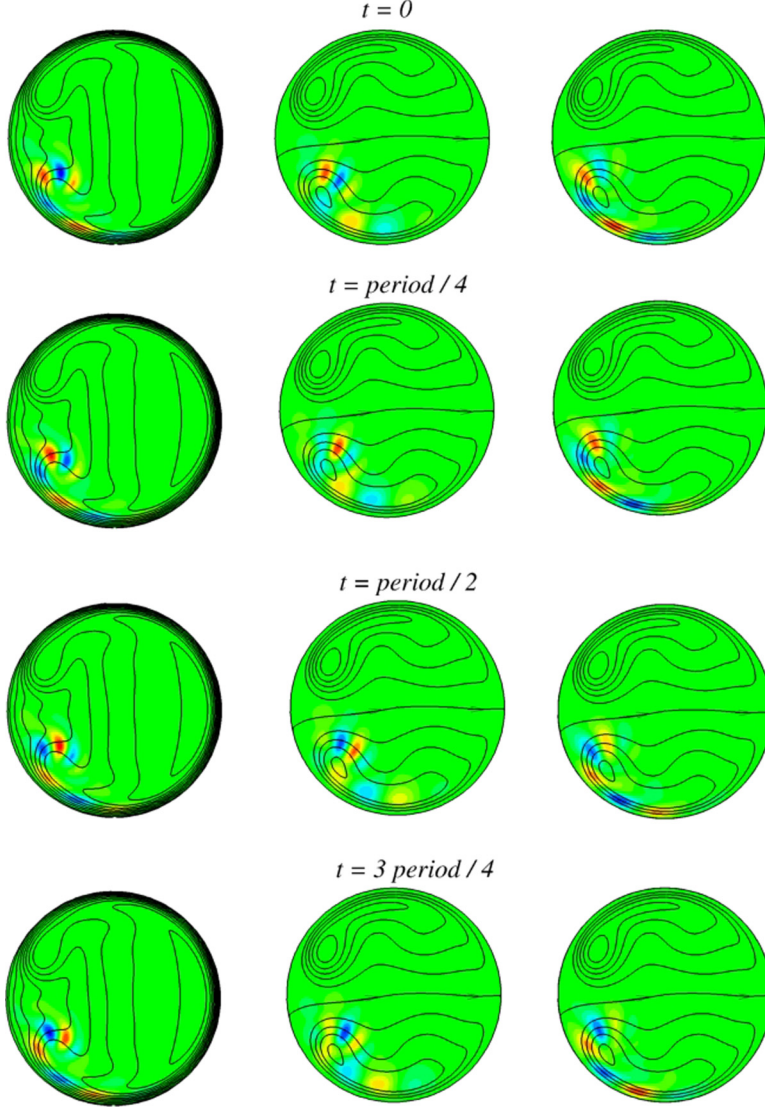
FIG. 19. Oscillations of the most unstable perturbation at $\varepsilon = 0.2$, $\lambda = 1.5$, $\mathrm{Re}_{\mathrm{cr}} = 1904$ (mode 4). Left frames: perturbation of the center line velocity superimposed with isolines of the base flow center line velocity (lines); center and right frames, respectively: perturbations of v_r and v_ξ superimposed with the pseudo-streamlines of base flow (lines). All the levels are equally spaced between the minimal and maximal values. Perturbation: $\max|\tilde{v}_s| = 0.0442$, $\max|\tilde{v}_r| = 0.0152$, $\max|\tilde{v}_\xi| = 0.0269$. Base flow: $\max|v_s| = 1.463$, $\psi_{\min} = -0.0455$, $\psi_{\max} = 0.0340$. Animation files: Perturbation_e=0p2_l=1p5.avi, Perturbation_e=0p1_l=1p5.avi.

weaker or completely disappears from the base flow (see animation for $\varepsilon = 0.2$, $\lambda = 5$). Thus, for the parameters of Fig. 21, the minimum and maximum values of the pseudo-streamfunction are approximately -0.15 and 0.06, so that the counterclockwise vortex is more than two times more intensive than the clockwise one. As is seen from the figures, this perturbation mode is characterized by two large-scale structures located in the dominant counterclockwise vortex. The perturbation of the center line velocity $\tilde{v}_s$ rotates in the clockwise direction around the dominant counterclockwise vortex (Fig. 20 and the corresponding animation), while evolution of the disturbances $\tilde{v}_r$ and $\tilde{v}_\xi$
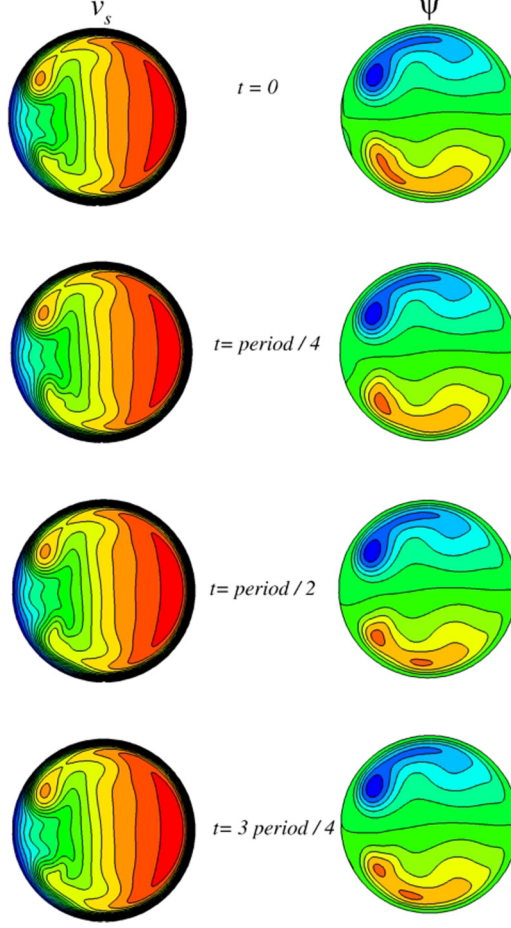
FIG. 20. Snapshots of a slightly supercritical oscillatory flow at $\varepsilon = 0.2$, $\lambda = 1.5$, $\mathrm{Re_{cr}} = 1904$. The levels are equally spaced between 0 and 1.4 for v_s and between -0.04 and 0.04 for ψ. Animation files: Flow_e=0p2_l=1.5.avi, Flow_e=0p1_l=1.5.avi.

cannot be easily connected to the direction of base flow motion. At larger torsions, however, the clockwise motion of these two perturbation components is clearly seen. The slightly supercritical flow at smaller torsions results in oscillation of both vortices and a weak clockwise rotational motion of the maximum isolines of the center line velocity v_s (Fig. 21 and the corresponding animations). During the oscillations period the Dean vortices size noticeably changes, which results also in strong oscillations of the zero pseudo-streamline. At larger torsions we observe oscillations of the single counterclockwise cross flow vortex, whose center also performs a weak clockwise rotational motion. Similarly to the previously described mode, we can characterize mode 5 as a large circumferential wave number upstream cross-flow wave.

The zeroing terms numerical experiment conducted for mode 5 showed that the instability is caused by interaction between disturbances u_ξ and u_s, and the base flow components V_s and V_ξ, while the radial velocity and its disturbance play only a passive role. Therefore, in this case we observe an instability of a swirling flow along the pipe center line.

An example of a similar, but downstream large circumferential wave number cross-flow wave is observed at larger curvatures $0.3 \leqslant \varepsilon \leqslant 0.6$, and large λ, and is characteristic for the rightmost branches of the corresponding neutral curves (Fig. 5). This perturbation branch is denoted as mode
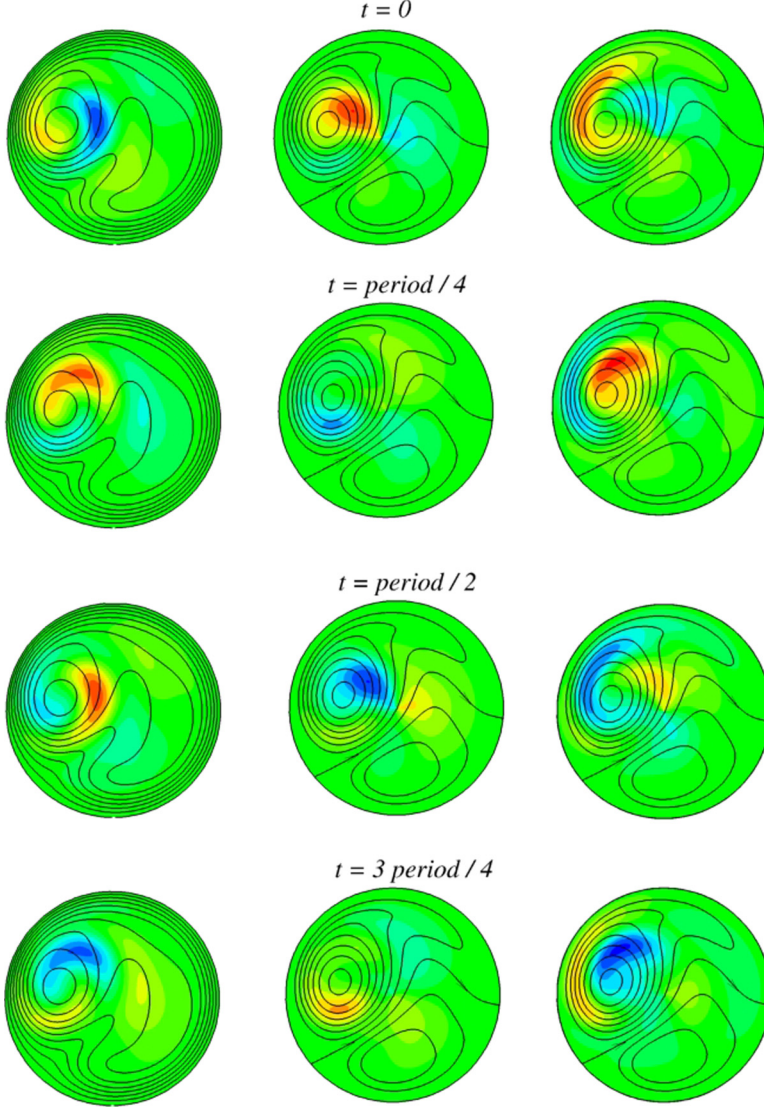
FIG. 21. Oscillations of the most unstable perturbation at $\varepsilon = 0.2$, $\lambda = 3$, $\mathrm{Re}_{\mathrm{cr}} = 449$ (mode 5). Left frames: perturbation of the center line velocity superimposed with isolines of the base flow center-ter line velocity (lines); center and right frames, respectively: perturbations of v_r and v_ξ superimposed with the pseudo-streamlines of base flow (lines). All the levels are equally spaced between the minimal and maximal values. Perturbation: $\max|\tilde{v}_s| = 0.0154$, $\max|\tilde{v}_r| = 0.00984$, $\max|\tilde{v}_\xi| = 0.0125$. Base flow: $\max|v_s| = 1.904$, $\psi_{\min} = -0.148$, $\psi_{\max} = 0.0614$. Animation files: Perturbation_e=0p2_l=3.avi, Perturbation_e=0p2_l=4.avi, Perturbation_e=0p2_l=5.avi.

7 and is depicted in Figs. 23 and 24. At the governing parameters of Figs. 23 and 24, the clockwise vortex is fully suppressed by the counterclockwise one, so that the base flow contains only a single Dean vortex. The perturbation consists of the large-scale structures similar to those of mode 5 (cf. Fig. 21 and Fig. 22), but contrary to mode 5 they rotate counterclockwise. In the resulting slightly supercritical flow we observe oscillations of the maximal values of both the center line velocity and pseudo-streamfunction. The maximum of v_s rotates counterclockwise together with the
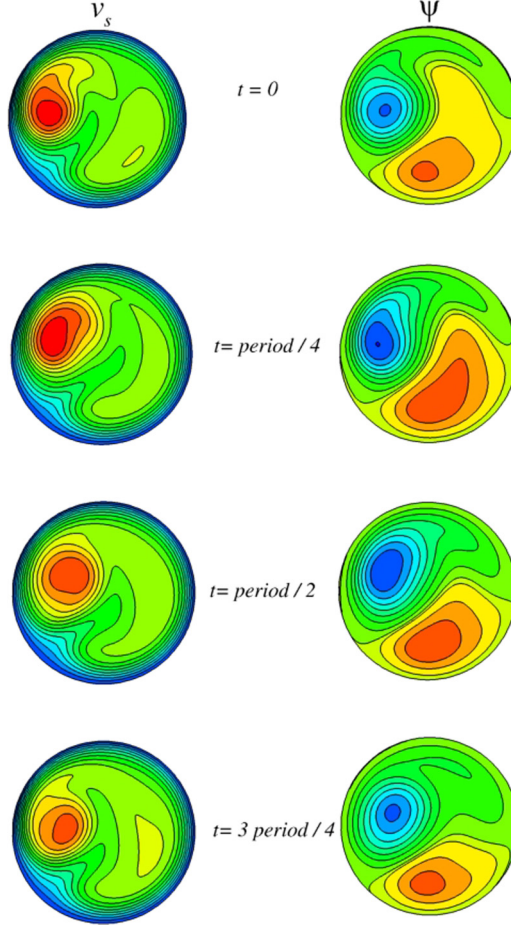
FIG. 22. Snapshots of a slightly supercritical oscillatory flow at $\varepsilon = 0.2$, $\lambda = 3$, $\mathrm{Re_{cr}} = 449$. The levels are equally spaced between 0 and 1.9 for v_s and between -0.16 and 0.07 for ψ. Animation files: Flow_e=0p2_l=3.avi, Flow_e=0p2_l=4.avi, Flow_e=0p2_l=5.avi.

perturbation, while the maximum of ψ remains almost motionless. The critical wave number and the critical frequency have the same sign in this case [Fig. 5(a) and 5(b)], so that an above assumed connection between the direction of the wave propagation along the center line and along the Dean vortex is supported. Contrary to the previous case, we cannot point on either term of the linearized equations that can be neglected without a change of the disturbances pattern or the eigenvalue. In spite of the fact that the instability in this case results in a quite simple streamwise swirling motion, its appearance includes interconnection of all the perturbations with all base flow components.

Perturbation mode 10 (not shown in figures) is characteristic for base flows in which the maximum of the center line velocity is shifted towards the inner pipe boundary, located on the left, due to advection by the dominant counterclockwise vortex (see corresponding animations). The perturbation pattern is a counterclockwise downstream traveling wave, similar to those observed for mode 7. Nevertheless, these modes are separated, as is clearly seen in Figs. 5(b) and 5(c), possibly because of the different size of the counterclockwise vortex. Also, slightly supercritical regimes of mode 10 involve oscillations of the weaker clockwise vortex, which is either too small or does not exist in the flows subject to instability due to mode 7. The zeroing terms numerical experiment shows that we cannot neglect any of the terms in the linearized equations. Also, the instability sets
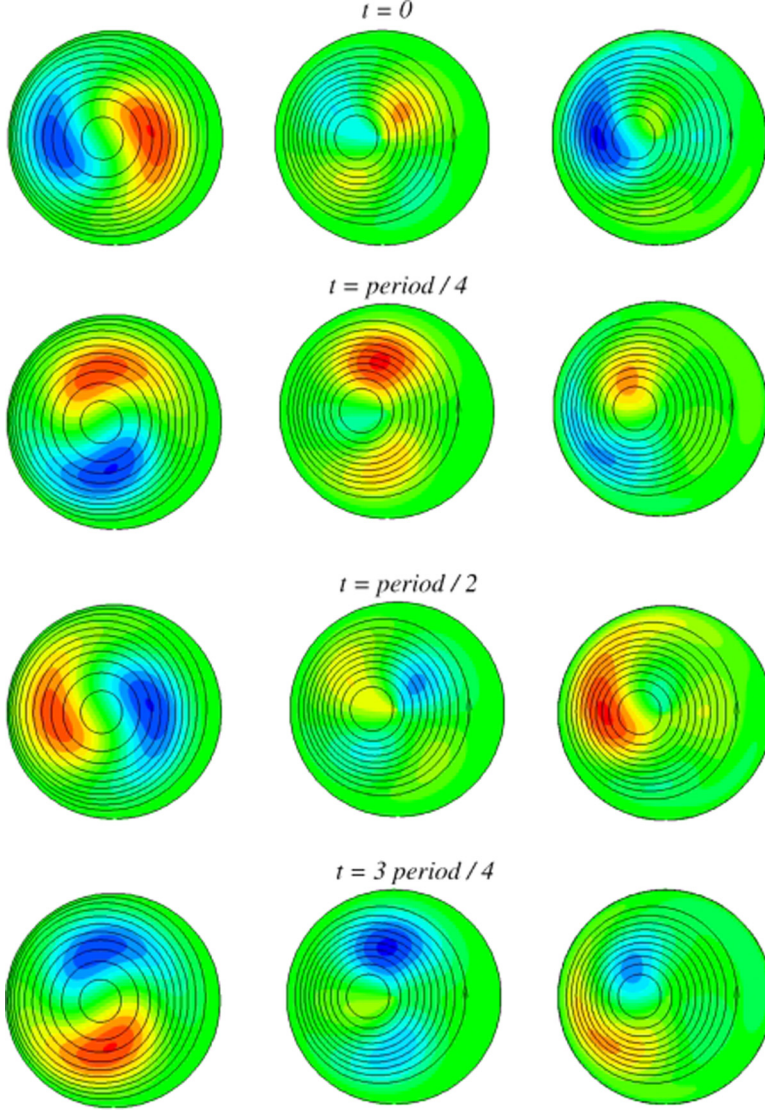
FIG. 23. Oscillations of the most unstable perturbation at $\varepsilon = 0.5$, $\lambda = 4$, $\mathrm{Re}_{\mathrm{cr}} = 360$ (mode 7). Left frames: perturbation of the center line velocity superimposed with isolines of the base flow center line velocity (lines); center and right frames, respectively: perturbations of v_r and v_ξ superimposed with the pseudo-streamlines of base flow (lines). All the levels are equally spaced between the minimal and maximal values. Perturbation: $\max|\tilde{v}_s| = 0.0102$, $\max|\tilde{v}_r| = 0.00267$, $\max|\tilde{v}_\xi| = 0.00362$. Base flow: $\max|v_s| = 2.082$, $\psi_{\min} = -1.092$, $\psi_{\max} = 0$. Animation files: Perturbation_e = 0p3_l = 4.avi, Perturbation_e = 0p4_l = 4.avi, Perturbation_e = 0p5_l = 4.avi, Perturbation_e = 0p6_l = 4.avi.

in at relatively low Reynolds number, so that no thin boundary layers are observed. Noticing that perturbations of the center line velocity rotate around the largest maximum of V_s, we examined the radial profile $V_s(r)$ passing through the maximum. This profile contains an inflection point, which can be an indication for a destabilization mechanism here.

For $0.4 \leqslant \varepsilon \leqslant 0.6$ modes 7 and 10 are separated by short intervals of λ, where the instability is caused by mode 11 (not shown in figures). Mode 11 seems to be similar to mode 10, but arising at larger torsions, so that the dominance of the counterclockwise vortex becomes more profound and
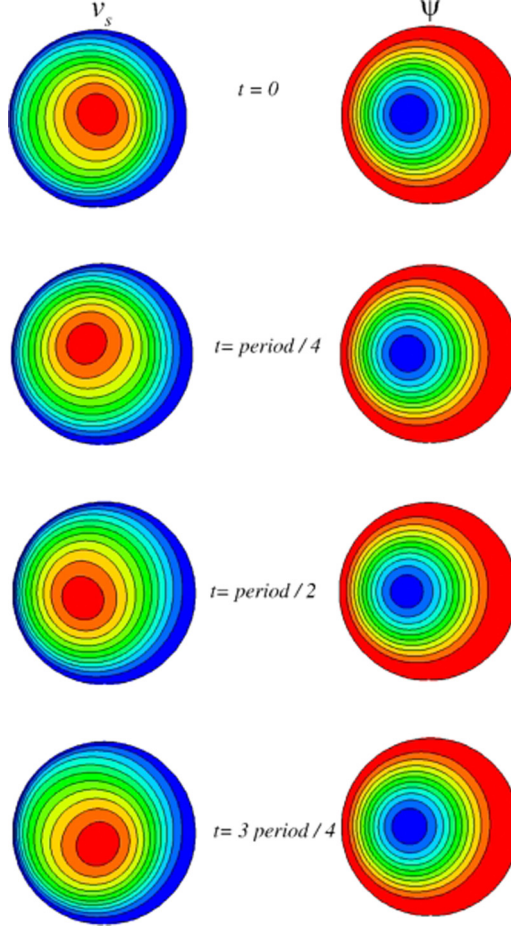
FIG. 24. Snapshots of a slightly supercritical oscillatory flow at $\varepsilon = 0.5$, $\lambda = 4$, $\mathrm{Re}_{\mathrm{cr}} = 360$. The levels are equally spaced between 0 and 2.0 for v_s and between -1.0 and -0.1 for ψ. Animation files: Flow_e $=$ 0p3_l $= 4$.avi, Flow_e $=$ 0p4_l $= 4$.avi, Flow_e $=$ 0p5_l $= 4$.avi, Flow_e $=$ 0p6_l $= 4$.avi.

the vortices become aligned vertically, and not horizontally, as it was for the zero torsion (Fig. 6 –12). There are several qualitative differences between modes 10 and 11. First, mode 11 sets in with the zero wave number, $k_{\mathrm{cr}} = 0$, so that the disturbances do not depend on the s coordinate. The oscillations are the same in every pipe cross section, and do not form a wave. The second difference follows from comparison of the perturbation amplitudes that form completely different patterns in the two cases. The third difference is that there is no inflection point on the $V_s(r)$ profile passing through the maximum of the center line velocity. The zeroing terms numerical experiment shows that we can neglect the terms $(\frac{u_\xi}{r}\frac{\partial V_s}{\partial \xi} + \frac{\varepsilon \sin(\xi)}{H_s} u_r V_s)\boldsymbol{e}_s$ and $\varepsilon \lambda u_s \frac{\partial V_r}{\partial \xi}\boldsymbol{e}_r$, but this does not help to understand the origin of this instability. A closer look at the base flow (see animations) shows that the maximum of V_s and the minimum of the pseudo-streamfunction are located close to each other. In the slightly supercritical regime the maximum of V_s makes a round motion around location of these two extremum points. Thus, one can assume that the perturbation of center line velocity is advected by the base flow around the dominant counterclockwise vortex, affecting in the same way two other velocity components. This assumption is supported by the corresponding animations.

V. CONCLUDING REMARKS

This study is based on the numerical approach validated in Ref. [7], and extends two particular examples of neutral stability curves reported there to a wide range of varying curvatures and torsions. The main result of this study is the map of stability of helical pipe flows reported in Fig. 5. These parametric results showing the dependence of the critical Reynolds number, critical wave number and critical frequency on the dimensionless curvature and torsion are presented for the first time. In all the cases considered, the instability sets in as a steady-oscillatory transition via a Hopf bifurcation.

The stability study needs an accurate calculation of the base steady flows. The convergence studies and comparison with independent experimental and numerical results were reported in Ref. [7] and are extended here by comparison with the experiments [23]. An accurate calculation of base steady flows allowed us to address the paradox of Ref. [24] and to provide some new arguments about dependence of the friction factor on the Reynolds and Dean numbers.

Along with this stability map, a graphical description of 13 distinct disturbance modes that become most unstable at different values of the curvature and torsion is presented. With only one exception of mode 10, these modes appear as traveling waves propagating downstream or upstream the base through flow. At small curvatures $\varepsilon \leqslant 0.2$ the instability always sets in as a downstream propagating traveling wave. With the increase of the pipe curvature we observe increase of the number of distinct most unstable modes replacing each other in the interval $0 \leqslant \lambda \leqslant 5$. These modes sometimes propagate upstream and sometimes are s-independent. They are classified by their symmetries, location, and direction of their propagation along the pipe and within its cross sections. Possible physical mechanisms exciting different perturbations and leading to qualitatively different supercritical oscillatory states are discussed. Based on examination of the perturbation patterns, we offered some explanation of these destabilizing processes that include instability of local viscous boundary, inviscid instability of mixing layers and/or shear through flow, as well as another self-sustained oscillatory process based on the interconnection between the Dean vortices and the through flow.

Two more comments should be made regarding current results on the stability of the helical pipe flow. First, starting from quite small dimensionless curvatures, of the order of 0.01, the instability develops in agreement with the linear stability theory, unlike the case of a straight circular pipe. This difference was mentioned also in Ref. [6], where it was confirmed by comparison with the experimental results for the zero torsion. The present results, together with comparisons with experiments made in Ref. [7], extend this conclusion for a nonzero torsion. At smaller curvatures $\varepsilon < 0.01$, the experimentally observed instability corresponds to a bypass transition similarly to the straight pipe [15,22,23]. Thus, studying the flow in a helical pipe with a gradually decreasing/increasing curvature may shed more light in physics of the bypass transition characteristic for the straight pipes and other shear flows. There is also a possibility to study an exchange between linear and bypass transition with variation of the pipe curvature.

The second comment relates to the multiplicity of possible perturbation modes. From the viewpoint of the bifurcation theory, there are points corresponding to the different Hopf bifurcations of codimension 2, e.g., Hopf-Hopf bifurcation [41] or tangent Hopf bifurcation [42]. These points can be easily found by the present numerical approach. Using flexible plastic pipes, one can easily alter the curvature and the torsion of a helical pipe in an experimental setup. Therefore, it yields a quite unique possibility to study bifurcations of higher codimension numerically and compare them with the experimental observations done at the prescribed governing parameters values.

to express his thanks to A. Cammi and A. Cioncolini for kindly agreeing to share their experimental results.

APPENDIX

For the "two-dimensional" flow depending only on the coordinates r and ξ, the momentum and continuity equations read as follows:

$$
\frac{\partial v_r}{\partial t} + v_r \frac{\partial v_r}{\partial r} + \frac{v_\xi}{r} \frac{\partial v_r}{\partial \xi} - \varepsilon\lambda \frac{v_s}{H_s} \frac{\partial v_r}{\partial \xi} - \frac{v_\xi^2}{r} - \frac{\varepsilon\sin(\xi)}{H_s} v_s^2
$$
$$
= -\frac{\partial p}{\partial r} + \frac{1}{R_G} \frac{1}{rH_s} \left\{ \frac{\partial^2}{\partial r^2}[rH_s v_r] + \frac{1}{r}\frac{\partial}{\partial \xi}\left[H_s \frac{\partial v_r}{\partial \xi}\right] + \varepsilon^2\lambda^2 r \frac{\partial}{\partial \xi}\left[\frac{1}{H_s}\frac{\partial v_r}{\partial \xi}\right] - \frac{1}{r}\frac{\partial v_\xi}{\partial \xi} - \varepsilon\lambda \frac{\partial}{\partial \xi}\left[\frac{v_s}{H_s}\right] \right\},
$$
(A1)

$$
\frac{\partial v_\xi}{\partial t} + \frac{v_r}{r}\frac{\partial(r v_\xi)}{\partial r} + \frac{v_\xi}{r}\frac{\partial v_\xi}{\partial \xi} - \varepsilon\lambda\frac{v_s}{H_s}\frac{\partial v_\xi}{\partial \xi} + \frac{v_\xi v_s}{r} - \frac{\varepsilon\cos(\xi)}{H_s}v_s^2
$$
$$
= -\frac{1}{r}\frac{\partial p}{\partial \xi} + \frac{1}{R_G}\frac{1}{H_s}\left\{ \frac{\partial}{\partial r}\left[\frac{H_s}{r}\frac{\partial(r v_\xi)}{\partial r}\right] + \frac{1}{r^2}\frac{\partial^2}{\partial \xi^2}[H_s v_\xi] + \varepsilon^2\lambda^2\frac{\partial}{\partial \xi}\left[\frac{1}{H_s}\frac{\partial v_\xi}{\partial \xi}\right] \right.
$$
$$
\left. + \frac{2}{r^2}\frac{\partial(H_s v_r)}{\partial \xi} + \varepsilon\cos(\xi)\frac{\partial v_r}{\partial r} + \varepsilon^2\lambda\frac{\partial}{\partial \xi}\left[\frac{\cos(\xi)}{H_s}v_s\right] \right\},
$$
(A2)

$$
\frac{\partial v_s}{\partial t} + v_r\frac{\partial v_s}{\partial r} + \frac{v_\xi}{r}\frac{\partial v_s}{\partial \xi} - \varepsilon\lambda\frac{v_s}{H_s}\frac{\partial v_s}{\partial \xi} + \frac{\varepsilon\sin(\xi)}{H_s}v_r v_s + \frac{\varepsilon\cos(\xi)}{H_s}v_\xi v_s
$$
$$
= -\frac{1}{H_s}\frac{\partial p}{\partial s} + \frac{1}{R_G}\left\{ \frac{1}{r}\frac{\partial}{\partial r}\left[\frac{r}{H_s}\frac{\partial(H_s v_s)}{\partial r}\right] + \frac{1}{r^2}\frac{\partial}{\partial \xi}\left[\frac{1}{H_s}\frac{\partial(H_s v_s)}{\partial \xi}\right] + \varepsilon^2\lambda^2\frac{\partial}{\partial \xi}\left[\frac{1}{H_s^2}\frac{\partial v_s}{\partial \xi}\right] \right.
$$
$$
\left. + \frac{\varepsilon^2\lambda\cos(\xi)}{r}\frac{\partial}{\partial r}\left[\frac{r^2}{H_s^2}v_r\right] - 2\varepsilon^2\lambda\frac{\partial}{\partial \xi}\left[\frac{\sin(\xi)}{H_s^2}v_r\right] - \varepsilon^2\lambda\frac{\partial}{\partial \xi}\left[\frac{\cos(\xi)}{H_s^2}v_\xi\right] \right\},
$$
(A3)

$$
\nabla \cdot \mathbf{v} = \frac{1}{rH_s}\left\{ \frac{\partial}{\partial r}[rH_s v_r] + \frac{\partial}{\partial \xi}[H_s v_\xi] - \varepsilon\lambda r\frac{\partial v_s}{\partial \xi} \right\} = 0.
$$
(A4)

The equations linearized near the steady-state flow $\{V_r(r,\xi), V_\xi(r,\xi), V_s(r,\xi), P(r,\xi)\}$ that govern infinitely small disturbances $\{u_r(r,\xi), u_\xi(r,\xi), u_s(r,\xi), p(r,\xi)\}\exp[i\sigma t + iks]$ are the following:

$$
\lambda u_r + V_r\frac{\partial u_r}{\partial r} + u_r\frac{\partial V_r}{\partial r} + \frac{V_\xi}{r}\frac{\partial u_r}{\partial \xi} + \frac{u_\xi}{r}\frac{\partial V_r}{\partial \xi} - \varepsilon\lambda u_s\frac{\partial V_r}{\partial \xi} + \frac{V_s}{H_s}\left[-\varepsilon\lambda\frac{\partial u_r}{\partial \xi} + iku_r\right]
$$
$$
- \frac{2V_\xi u_\xi}{r} - \frac{2\varepsilon\sin(\xi)}{H_s}V_s u_s
$$
$$
= -\frac{\partial p}{\partial r} + \frac{1}{R_G}\frac{1}{rH_s}\left\{ \frac{\partial^2}{\partial r^2}[rH_s u_r] + \frac{1}{r}\frac{\partial}{\partial \xi}\left[H_s\frac{\partial u_r}{\partial \xi}\right] + \varepsilon^2\lambda^2 r\frac{\partial}{\partial \xi}\left[\frac{1}{H_s}\frac{\partial u_r}{\partial \xi}\right] - \frac{1}{r}\frac{\partial u_\xi}{\partial \xi} - \varepsilon\lambda\frac{\partial}{\partial \xi}\left[\frac{u_s}{H_s}\right] \right.
$$
$$
\left. - k^2\frac{ru_r}{H_s} - ik\varepsilon\lambda r\frac{\partial}{\partial \xi}\left[\frac{u_r}{H_s}\right] - \frac{ikr}{H_s}\varepsilon\lambda\frac{\partial u_r}{\partial \xi} + \frac{ik}{H_s}u_s \right\},
$$
(A5)

$$
\lambda u_\xi + \frac{V_r}{r}\frac{\partial u_\xi}{\partial r} + \frac{u_r}{r}\frac{\partial V_\xi}{\partial r} + \frac{V_\xi}{r}\frac{\partial u_\xi}{\partial \xi} + \frac{u_\xi}{r}\frac{\partial V_\xi}{\partial \xi} - \varepsilon\lambda\frac{V_s}{H_s}\frac{\partial u_\xi}{\partial \xi} - \varepsilon\lambda\frac{u_s}{H_s}\frac{\partial V_\xi}{\partial \xi} + \frac{V_\xi u_s}{r}
$$
$$
+ \frac{u_\xi V_s}{r} - \frac{2\varepsilon\cos(\xi)}{H_s}V_s u_s + \frac{ik}{H_s}V_s u_\xi
$$
$$
= -\frac{1}{r}\frac{\partial p}{\partial \xi} + \frac{1}{R_G}\frac{1}{H_s}\left\{ \frac{\partial}{\partial r}\left[\frac{H_s}{r}\frac{\partial(r u_\xi)}{\partial r}\right] + \frac{1}{r^2}\frac{\partial^2}{\partial \xi^2}[H_s u_\xi] + \varepsilon^2\lambda^2\frac{\partial}{\partial \xi}\left[\frac{1}{H_s}\frac{\partial u_\xi}{\partial \xi}\right] + \frac{2}{r^2}\frac{\partial(H_s u_r)}{\partial \xi} \right.
$$

$$+ \varepsilon \cos(\xi) \frac{\partial u_r}{\partial r} + \varepsilon^2 \lambda \frac{\partial}{\partial \xi} \left[\frac{\cos(\xi)}{H_s} u_s \right] - k^2 \frac{u_\xi}{H_s} - ik\varepsilon\lambda \frac{\partial}{\partial \xi} \left[\frac{u_\xi}{H_s} \right] - \frac{ik}{H_s} \varepsilon\lambda \frac{\partial u_\xi}{\partial \xi} - ik\varepsilon\cos(\xi) \frac{u_s}{H_s} \bigg\},$$

(A6)

$$\lambda v_s + V_r \frac{\partial u_s}{\partial r} + u_r \frac{\partial V_s}{\partial r} + \frac{V_\xi}{r} \frac{\partial u_s}{\partial \xi} + \frac{u_\xi}{r} \frac{\partial V_s}{\partial \xi} - \varepsilon\lambda \frac{V_s}{H_s} \frac{\partial u_s}{\partial \xi} - \varepsilon\lambda \frac{u_s}{H_s} \frac{\partial V_s}{\partial \xi} + \frac{\varepsilon\sin(\xi)}{H_s}(V_r u_s + u_r V_s)$$

$$+ \frac{\varepsilon\cos(\xi)}{H_s}(V_\xi u_s + u_\xi V_s) + \frac{ik}{H_s} V_s u_s$$

$$= \frac{\varepsilon\lambda}{H_s} \frac{\partial p}{\partial \xi} - \frac{ik}{H_s} p + \frac{1}{R_G} \left\{ \frac{1}{r} \frac{\partial}{\partial r} \left[\frac{r}{H_s} \frac{\partial (H_s u_s)}{\partial r} \right] + \frac{1}{r^2} \frac{\partial}{\partial \xi} \left[\frac{1}{H_s} \frac{\partial (H_s u_s)}{\partial \xi} \right] + \varepsilon^2 \lambda^2 \frac{\partial}{\partial \xi} \left[\frac{1}{H_s^2} \frac{\partial u_s}{\partial \xi} \right]$$

$$+ \frac{\varepsilon^2 \lambda \cos(\xi)}{r} \frac{\partial}{\partial r} \left[\frac{r^2}{H_s^2} u_r \right] - 2\varepsilon^2 \lambda \frac{\partial}{\partial \xi} \left[\frac{\sin(\xi)}{H_s^2} u_r \right] - \varepsilon^2 \lambda \frac{\partial}{\partial \xi} \left[\frac{\cos(\xi)}{H_s} u_\xi \right]$$

$$- \frac{ik}{r} \frac{\partial}{\partial \xi} \left[\frac{r}{H_s} u_\xi \right] - \frac{ik}{r} \frac{\partial}{\partial r} \left[\frac{r}{H_s} u_r \right] \bigg\},$$

(A7)

$$\nabla \cdot \tilde{\boldsymbol{v}} = \frac{1}{rH_s} \left\{ \frac{\partial}{\partial r}[rH_s \tilde{v}_r] + \frac{\partial}{\partial \xi}[H_s \tilde{v}_\xi] - \varepsilon\lambda r \frac{\partial \tilde{v}_s}{\partial \xi} + ik\tilde{v}_s \right\} = 0.$$

(A8)

[1] C. M. White, Streamline flow through curved pipes, Proc. Roy. Soc. London **123**, 645 (1929).

[2] G. I. Taylor, The criterion for turbulence in curved pipes, Proc. Roy. Soc. London **24**, 243 (1929).

[3] W. R. Dean, Note on the motion of fluid in a curved pipe, Phil Mag. **4**, 208 (1927).

[4] S. Vadhisth, V. Kumar, and K. D. P. Nigam, A review of the potential applications of curved geometries in process industry, Ind. Eng. Chem. Res. **47**, 3291 (2016).

[5] H. Salven, F. W. Cotton, and C. E. Grosch, Linear stability of Poiseuille flow in a circular pipe, J. Fluid Mech. **98**, 273 (1980).

[6] J. Canton, P. Schlatter, and R. Örlü, Modal instability of the flow in a toroidal pipe, J. Fluid Mech. **792**, 894 (2016).

[7] A. Gelfgat, A comparative study on instability of steady flows in helical pipes, Fluid Dyn. Res. **52**, 015511 (2020).

[8] M. Germano, On the effect of torsion on a helical pipe flow, J. Fluid Mech. **125**, 1 (1982).

[9] K. Yamamoto, S. Yanase, and T. Yoshida, Torsion effect on the flow in a helical pipe, Fluid Dyn. Res. **14** 259 (1994).

[10] T. J. Hüttl and R. Friedrich, Influence of curvature and torsion on turbulent flow in helically coiled pipes, Int. J. Heat Fluid Flow **21**, 345 (2000).

[11] A. Y. Gelfgat, A. L. Yarin, and P. Z. Bar-Yoseph, Dean vortices–induced enhancement of mass transfer through an interface separating two immiscible liquids, Phys. Fluids **15**, 330 (2003).

[12] M. R. H. Nobari and A. Malvandi, Torsion and curvature effects on fluid flow in a helical annulus, Int. J. Non-Linear Mech. **57**, 90 (2013).

[13] A. F. Totorean, S. I. Bernad, and R. F. Susan-Resiga, Fluid dynamics in helical geometries with application for by-pass grafts, Appl. Math. Comput. **272**, 604 (2016).

[14] A. Y. Gelfgat, Three-dimensional instability of axisymmetric flows, solution of benchmark problems by a low-order finite volume method, Int. J. Numer. Meths. Fluids **54**, 269 (2007).

[15] K. R. Sreenivasan and P. J. Strykowski, Stabilization effects in flow through helically coiled pipes, Exp. Fluids **1**, 31 (1983).

[16] D. R. Webster and J. A. C. Humphrey, Experimental observation of flow instability in a helical coil, J. Fluids Eng. **115**, 436 (1993).

[17] K. Yamamoto, S. Yanase, and R. Jiang, Stability of the flow in a helical tube, Fluid Dyn. Res. **22** 153 (1998).

[18] J. Kühnen, M. Holzner, B. Hof, and H. C. Kuhlmann, Experimental investigation of transitional flow in a toroidal pipe, J. Fluid Mech. **738**, 463 (2014).

[19] J. Kühnen, P. Braunshier, P. Scwegel, H. C. Kuhlmann, and B. Hof, Subcritical versus supercritical transition to turbulence in curved pipes, J. Fluid Mech. **770**, R3-1 (2015).

[20] D. R. Webster and J. A. C. Humphrey, Traveling wave instability in helical coil flow, Phys. Fluids **9**, 407 (1997).

[21] I. Di Piazza and M. Ciofalo, Transition to turbulence in toroidal pipes, J. Fluid Mech. **687**, 72 (2011).

[22] J. De Amicis, A. Cammi, L. P. M. Colombo, M. Colombo, and M. E. Ricotti, Experimental and numerical study of the laminar flow in helically coiled pipes, Progr. Nuclear Energy **76**, 206 (2014).

[23] A. Cioncolini and L. Santini, An experimental investigation regarding the laminar to turbulent flow transition in helically coiled pipes, Exp. Thermal Fluid Sci. **30**, 367 (2006).

[24] R. Ramshankar and K.R. Sreenivasan, A paradox concerning the extended Stokes series solution for the pressure drop in coiled pipes, Phys. Fluids **31**, 1339 (1988).

[25] A. Y. Gelfgat and P. Z. Bar-Yoseph, Multiple solutions and stability of confined convective and swirling flows—A continuing challenge, Int. J. Numer. Meths. Heat Fluid Flows **14**, 213 (2004).

[26] A. Y. Gelfgat, Visualization of three-dimensional incompressible flows by quasi-two-dimensional divergence-free projections in arbitrary flow regions, Theor. Comput. Fluid Dyn. **30**, 339 (2016).

[27] See Supplemental Material at http://link.aps.org/supplemental/10.1103/PhysRevFluids.5.103904 for a table with the animation files.

[28] C. Y. Wang, On the low-Reynolds-number flow in a helical pipe, J. Fluid Mech. **108**, 185 (1981).

[29] R. B. Lechouq, D. C. Sorensen, and C. Yang, *ARPACK Users' Guide, Solution of Large Scale Eigenvalue Problems with Implicitly Restarted Arnoldi Methods* (SIAM, Philadelphia, 1998).

[30] D. Hassard, N. D. Kazarinoff, and Y.-H. Wan, *Theory and Applications of Hopf Bifurcation*, London Mat. Soc. Lecture Notes Series, Vol. 41 (Cambridge University Press, Cambridge, 1981).

[31] F. S. Godeferd, C. Cambon, and S. Leblanc, Zonal approach to centrifugal, elliptic and hyperbolic instabilities in Stuart vortices with external rotation, J. Fluid Mech. **449**, 1 (2001).

[32] J.-M. Chomaz, S. Ortiz, S. Le Dizés, and P. Billant, Stability of quasi two-dimensional vortices, Lect. Notes Phys. **805**, 35 (2010).

[33] G. F. Carnevale, R. C. Kloosterziel, and P. Orlandi, Equilibration of centrifugally unstable vortices: A review, Eur. J. Mech. B/Fluids **55**, 246 (2016).

[34] P. Billant, Three-dimensional stabiltiy of a vortex pair, Phys. Fluids **11**, 2069 (1999).

[35] C. Roy, N. Schaeffer, S. Le Dizés, and M. Thomson, Stability of pair of co-rotating vortices with axial flow, Phys. Fluids **20**, 094101 (2008).

[36] T. Leweke, S. Le Dizés, and C. H. K. Williamson, Dynamics and instabilities of vortex pairs, Ann. Rev. Fluid Mech. **48**, 507 (2016).

[37] C. Gargan-Shingles, M. Rudman, and K. Ryan, The linear stability of swirling vortex rings, Phys. Fluids **28**, 114106 (2016).

[38] A. Y. Gelfgat, Destabilization of convection by weak rotation, J. Fluid Mech. **685**, 377 (2011).

[39] D. Nagarathinam, A. Sameen, and M. Mathur, Centrifugal instability in non-axisymmetric vortices, J. Fluid Mech. **769**, 26 (2015).

[40] A. Y. Gelfgat and Kit E.Spatial versus temporal instabilities in a parametrically forced stratified mixing layer, J. Fluid Mech. **552**, 189 (2006).

[41] Y. A. Kuznetsov, *Elements of Applied Bifurcation Theory* (Springer, New York, 1998).

[42] F. Marques, A. Y. Gelfgat, and J. M. Lopez, Tangent double Hopf bifurcation in a differentially rotating cylinder flow, Phys. Rev. E **68**, 016310 (2003).